PHYSICAL REVIEW C **87**, 054622 (2013)

Determination of the coexistence curve, critical temperature, density, and pressure of bulk nuclear matter from fragment emission data

J. B. Elliott,[1,*] P. T. Lake,[2] L. G. Moretto,[2] and L. Phair[2]

[1]*Lawrence Livermore National Laboratory, 7000 East Avenue, Livermore, California 94550, USA*

[2]*Lawrence Berkeley National Laboratory, 1 Cyclotron Road, Berkeley, California 94720, USA*

(Received 12 February 2013; published 30 May 2013)

An analysis of six different sets of experimental data indicates that infinite, neutron-proton symmetric, neutral nuclear matter has a critical temperature of $T_c = 17.9 \pm 0.4$ MeV, a critical density of $\rho_c = 0.06 \pm 0.01$ nucleons/fm^3, and a critical pressure of $p_c = 0.31 \pm 0.07$ MeV/fm^3. These values have been obtained by analyzing data from six different reactions studied in three experiments: two "compound nuclear" reactions, ^{58}Ni $+^{12}$ C $\rightarrow ^{70}$Se and ^{64}Ni $+^{12}$ C $\rightarrow ^{76}$Se (both performed at the LBNL 88-in. cyclotron); and four "multifragmentation" reactions, 1 GeV/c $\pi+^{197}$Au (performed by the Indiana Silicon Sphere Collaboration), 1 GeV/nucleon ^{197}Au+^{12}C, 1 GeV/nucleon ^{139}La+^{12}C, and 1 GeV/nucleon ^{84}Kr+^{12}C (all performed by the Equation of State Collaboration). The charge yields of all reactions as a function of the excitation energy were fit with a version of Fisher's droplet model modified to account for the dual components of the fluid (i.e., protons and neutrons), Coulomb effects, finite-size effects, and angular momentum arising from the nuclear collisions.

DOI: 10.1103/PhysRevC.87.054622 PACS number(s): 25.70.Mn, 05.70.Jk, 25.70.Pq, 24.60.Ky

I. INTRODUCTION

In the long history of the study of the liquid-to-vapor phase transition of nuclear matter [1–14] various investigations have sought to determine one or more critical exponents [1,4,10–12,14], other studies have examined caloric curves [5], and others have reported the observation of negative heat capacities [9]. All of these efforts suffer from the lack of knowledge of the systems location in pressure-density-temperature (p, ρ, T) space. Specifically, interpretations of caloric curves and negative heat capacities depend on assumptions of either constant pressure or constant density [15,16]. In determining critical exponents, it was assumed that the systems were at coexistence and that the surface energy was the single, dominant factor. Furthermore, in those efforts, finite-size effects were not considered.

The analysis presented here makes no assumptions about the location of the system in (p, ρ, T) space and accounts specifically for effects such as Coulomb, angular momentum and finite size. Our approach begins by considering nuclei as drops of an hypothetical nuclear fluid. The liquid drop model [17] takes up this idea quantitatively. The approximately constant binding energy per particle in heavier nuclei suggests that this fluid is bound together by a saturating short-range force similar to that acting between the molecules of simple fluids (i.e., van der Waals like).

Present-day formulations of the liquid drop model [18,19] express the binding energy in terms of a volume term proportional to the number of nucleons A and corrected for finiteness by means of an expansion in terms of $A^{-1/3}$ of which only the first (surface energy) order term is kept. Additional corrections are added to account for neutron/proton asymmetry, Coulomb interactions, and pairing effects.

Global fits to nuclear masses lead, on the one hand, to a reproduction of binding energies to within 1% ($\lesssim$10 MeV) and, on the other, to the characterization of the hypothetical fluid mentioned above, where finiteness, neutron/proton asymmetry, and Coulomb interactions have been removed. This is the "bulk nuclear matter" which has been studied theoretically over the history of nuclear physics.

Van der Waals fluids admit various phases, among which are the vapor and the liquid. Thermodynamically, the equilibrium coexistence of these phases and the associated liquid-vapor phase transition are well understood. The van der Waals aspects of the nuclear binding energy lead naturally to the question: Does nuclear matter sustain a vapor phase as well as the condensed liquid phase? In the phase diagram is there a (first-order) coexistence line terminating at a critical point [1]? and if so, how can one obtain such information experimentally? We answer these questions (in the affirmative) and determine the coexistence curve and critical point of bulk nuclear matter from data obtained in three experiments and six different reactions.

In this paper, we first describe a physical picture of the nuclear reactions in question in Sec. II. Then we provide a brief description of the experiments in Sec. III. Greater detail about the experiments can be found in the references provided. Next, in Sec. IV, we give a detailed description of the theory and analysis used on the experimental data. Finally, in Sec. V, we use the results of that analysis to determine the coexistence curve and critical point of bulk nuclear matter.

II. THE PHYSICAL PICTURE

Thermal nuclear sources (compound nuclei and higher energy nuclear aggregates) emit particles such as neutrons, protons, and heavier charged fragments into vacuum in a process that is very similar to evaporation [20]. This type of emission from thermal, equilibrated systems is in contrast to the direct, or prompt, particle emission from excited nuclear systems that are out of equilibrium.

*elliott38@llnl.gov

For fluid systems like water, evaporation rates allow one to recover the properties of the saturated vapor in equilibrium [21]. However, in nuclear systems, finiteness and the presence of Coulomb effects prevent such a simple approach to the characterization of the phase diagram.

It has been shown previously how it is possible to "reduce" the nuclear evaporation rate to that of an infinite, uncharged symmetric fluid: finiteness is accounted for in terms of the "complement" approach [22], Coulomb effects can similarly be factored out [23], and the corrected rates can then be related to the properties of the hypothetical nuclear matter vapor [21].

We demonstrate explicitly how properties of the bulk nuclear matter such as its phase diagram can be ascertained from experimental measurements of fragment distributions starting with a physical picture of fragment production from excited nuclei. This will illustrate how one can talk about coexistence without the vapor being present and how an equilibrium description, such as Fisher's theory [24,25] (described in Sec. IV A), is relevant to the free vacuum decay of an evaporating, nuclear system [22].

Thermodynamicians would determine a phase diagram via direct measurements of the pressure, density, and temperature of their fluid. Unfortunately, such direct measurements of the temperature, density, and pressure for a nuclear fluid are not sensible. However, the measurement of clusters in nuclear reactions has been easily achieved and has a long tradition. Thus, we believe that in nuclear physics, this is the royal avenue toward the extraction of the phase diagram.

Let us consider a liquid in equilibrium with its saturated vapor. At equilibrium, any particle evaporated by the liquid is restored on average by the vapor bombarding it. In other words, the outward evaporation flux from the liquid to the vapor is matched by the inward condensation flux. This is true for any kind of evaporated particle. The vapor acts as a mirror that reflects the evaporated particles back into the liquid.

One could probe the saturated vapor by putting a detector in contact with it. However, because the outward and inward fluxes are identically the same at equilibrium, putting the detector in contact with the liquid also probes the vapor. Therefore, we do not need the vapor to be physically present in order to characterize it completely. We can study the evaporation of the liquid and dispense with the surrounding saturated vapor. In these situations one thinks of a *virtual vapor*, realizing that first-order phase transitions depend exclusively on the intrinsic properties of the two phases, and not on their interaction. Of course, if the vapor is not there to restore the emitting system with its return flux, evaporation will proceed and the system will cool.

An excited nucleus is a small drop of equilibrated nuclear matter that emits neutrons, protons, and higher charged fragments into vacuum according to statistical decay rate theory. In this picture there is no surrounding vapor, no confining box, and no need for either. As described in the preceding paragraph, by studying the outward flux of the *first* fragments emitted from a thermal source at equilibrium, we can study the nature of the vapor even when it is absent (the virtual vapor).

Quantitatively, the concentration $n_{A_f}(T)$ of any species with A_f constituents at temperature T in the vapor is related to the corresponding decay rate $R_{A_f}(T)$ [or to the decay width $\Gamma_{A_f}(T)$] from the nucleus by matching the evaporation and condensation fluxes,

$$R_{A_f}(T) = \frac{\Gamma_{A_f}(T)}{\hbar} \approx n_{A_f}(T)\langle v_{A_f}(T) 4\sigma_{\rm inv}(v_{A_f})\rangle, \qquad (1)$$

where $v_{A_f}(T)$ is the thermal velocity of species A_f (of order $\sqrt{T/A_f}$) crossing the nuclear interface represented by the cross section $\sigma_{\rm inv}$ (of order $A_s^{2/3}$, where A_s is the mass number of the evaporating nucleus); T is the temperature of the equilibrated, excited nucleus when the first fragment is emitted; $\hbar$ is Planck's constant; and Coulomb effects have been, for the time being, neglected (they are dealt with below).

Equation (1) shows the fundamental and simple connection between the (compound nucleus) decay rate and the fragment concentration in the vapor. Thus, the vapor phase in equilibrium can be completely characterized in terms of the decay rate.

The physical picture described above is valid instantaneously. The result of successive evaporation in vacuum leads to abundances of various species of emitted fragments that arise from a continuum of systems at different temperatures [26]. This leads to complications in various thermometers: kinetic energy, isotope ratios, etc.

Our way of avoiding this complication is to consider only fragments that are emitted very rarely so that, if they are not emitted first, they are effectively not emitted at all. In other words, we consider only fragments that, by virtue of their high surface energy (and high charge), have a high emission barrier. The rapidly increasing Coulomb barrier with fragment charge Z strongly enhances this effect. Thus the lower cutoff of about $Z \approx 6$ is used in the analysis that follows.

III. EXPERIMENTS

The above physical picture is used here to analyze the data from two kinds of experiments: compound nuclear decay and multifragmentation. Both types of experiments measure the total yield or number of fragments emitted from a thermal nuclear source, $Y_{Z_f}(E_s^*)$, as a function of the excitation energy of the source, E_s^*, and charge of the fragment, Z_f. For both types of experiments it is assumed that the collisions produce an excited, equilibrated thermal source of radius r_s consisting of A_s nucleons (Z_s protons and N_s neutrons) at excitation energy E_s^* and with angular momentum $\vec{I}$. This is the initial state of the system: an excited, thermal nucleus which emits neutrons, protons, and heavier charged fragments.

A. Compound-nucleus experiments

The first kind of experiment gives rise to a *compound nucleus*. A compound nucleus is formed when one nucleus impacts another nucleus and the two combine to form a single, compound system. The nucleon number and charge of the compound nucleus are just the sum of the nucleon number and charge of the two colliding nucleii. Its excitation energy can be determined from the energy of the bombarding nuclei and the masses of the target and projectile. The excited compound

nucleus is a thermal source that emits protons, neutrons, and other heavier charged fragments.

The compound nucleus experiments analyzed here were performed at the 88-in. cyclotron of the Lawrence Berkeley National Laboratory [27]. An advanced electron-cyclotron-resonance (AECR) ion source [28] was utilized to produce highly charged ^{58}Ni and ^{64}Ni ions, which, after injection into the cyclotron and acceleration to the desired energy, impinged on a high-purity [29,38] carbon target (1.0 mg/cm^2). The fragments emitted in the reactions were detected in two position-sensitive $\Delta E - E$ detector assemblies placed on either side of the beam. The methods of the energy and position calibrations of the ΔE and E detectors have been described previously [29,30].

B. Nuclear multifragmentation experiments

The second kind of experiment analyzed in this work gives rise to a phenomenon called *multifragmentation* [7,31–37]. In a multifragmentation experiment, one nucleus is accelerated to a high velocity and impacts another nucleus, and in the experiments considered here, one of the colliding nuclei is larger than the other. Typically, the collision between nuclei in multifragmentation experiments is more violent than that in compound-nucleus experiments. Either the two nuclei partially fuse or a "fireball" is generated from the occluded parts of the target and projectile. The larger of the two nuclei promptly loses nucleons during the collision, leading to an excited, thermal remnant with a smaller nucleon number and lower charge than the initial nuclei. In the experiments considered here, the higher the excitation energy of the remnant, the smaller the nucleon number and charge of the remnant. Figure 1 shows the nucleon number, A_s, and charge, Z_s, as a function of the excitation energy, E_s^*, for the remnants created in the multifragmentation experiments considered here. The excited remnant is a thermal source that emits protons, neutrons, and other heavier charged fragments just like an ordinary compound nucleus. In multifragmentation experiments, the excitation energy is estimated from measurements of the kinetic energy of the fragments emitted from the remnant and other considerations [38,39].

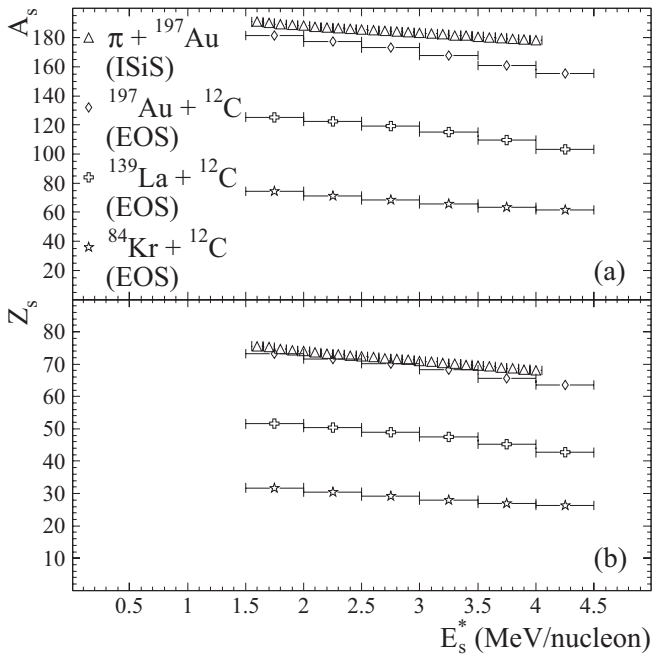

FIG. 1. (a) Nucleon number, A_s, as a function of excitation energy, E_s^*, for the thermal sources created by the multifragmentation experiments. (b) Charge, Z_s, of the thermal source as a function of excitation energy.

1. Equation of state (EOS) experiments

Three sets of multifragmentation data analyzed here are from the reactions 1 GeV/nucleon ^{197}Au+^{12}C,

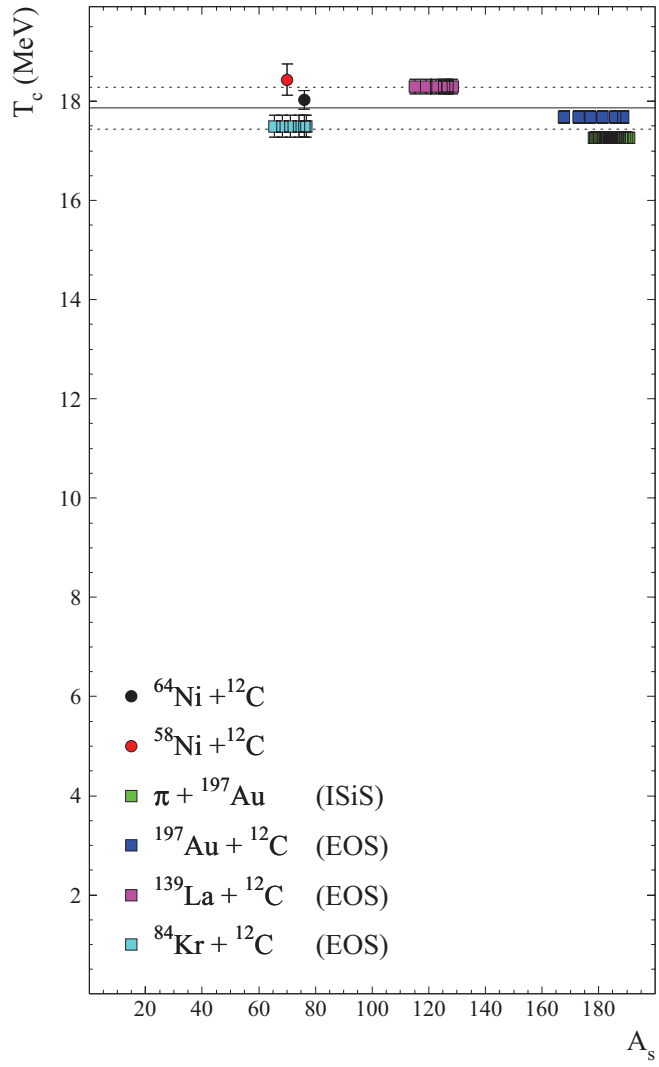

FIG. 2. (Color online) The critical temperature as a function of the thermal source mass. Results of the compound-nucleus reactions are shown by circles and results of multifragmentation reactions are shown by squares. Colors show results for different experiments. The solid line shows the average of all the measurements and the dotted lines show the RMS variation: 17.9 ± 0.4 MeV. There are multiple points for the multifragmentation reactions owing to the multiple source sizes in the experiments as shown in Fig. 1.

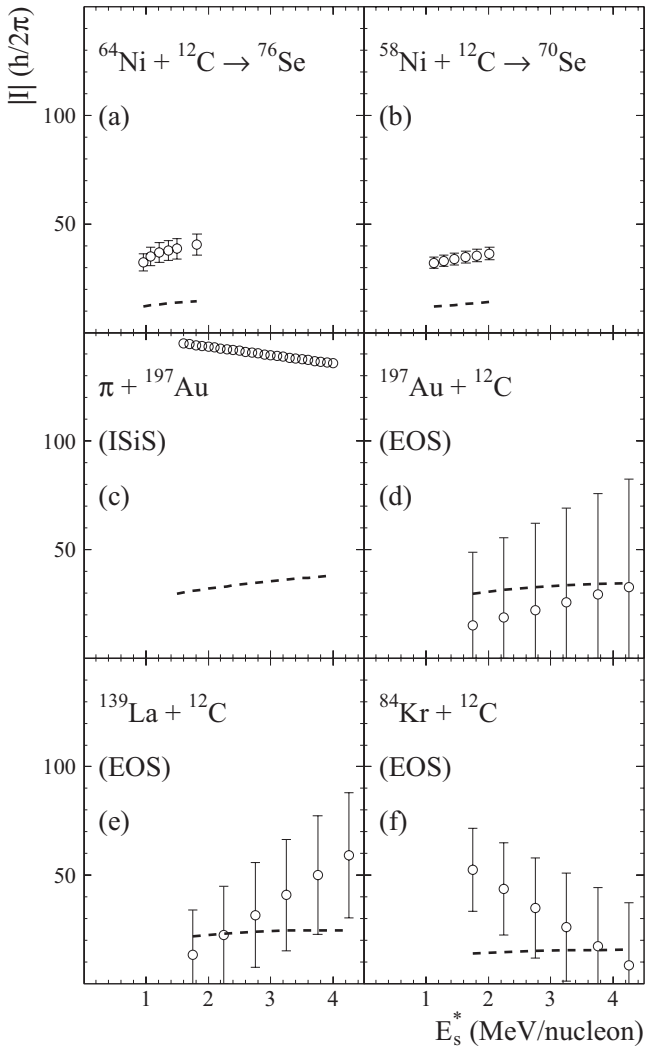

FIG. 3. Angular momentum values for all six reactions predicted by the fitting of the charge yields. Error bars are smaller than the points for the ISiS experiments. The dashed line shows a thermal estimate of the angular momentum [83]. See text for details.

1 GeV/nucleon ^{139}La+^{12}C, and 1 GeV/nucleon ^{84}Kr+^{12}C and were collected by the EOS Collaboration at the Lawrence Berkeley National Laboratory Bevalac. This experiment studied the projectile fragmentation and detected nearly all of the charged reaction products on an event-by-event basis [4,38–40]. Charged particles with charges of from 1 to 6 were identified using a time projection chamber [41], while a multiple-sampling ionization chamber detected charged particles with charges from 7 to 79 [42].

2. *Indiana Silicon Sphere (ISiS) experiment*

The other multifragmentation data analyzed here are from the reaction 1 GeV/c π+^{197}Au and were collected by the ISiS Collaboration at the Alternating Gradient Synchrotron (AGS) at Brookhaven National Laboratory [37,43–46]. The AGS provided beams of 1 GeV/c π incident on a gold target. Particles with charges from 1 to 16 were measured by the ISiS 4π detector array [43], providing a high-statistics, exclusive data set with finer bins in excitation energy than the EOS experiment [44].

IV. ANALYSIS

We now provide a derivation of a formula for the average fragment yields, $Y_{Z_f}(E^*_s)$, based on the initial state of the system (the excited, compound nucleus or remnant) and the final state of the system (the fragment and its complement). This has the advantage of explicitly dealing with the effects of the finite size of the systems we study here. We start from Fisher's droplet model [24,25] and modify it to account for effects that arise from finite size [22], Coulomb [23], isospin, angular momentum, and secondary decay of excited fragments. *These modifications, coupled with the explicit treatment of finite-size effects, make it so that the parameters that are extracted from our analysis (e.g.,*T_c*) reflect the values for infinite, neutron-proton-symmetric, neutral nuclear matter.*

A. Fisher's droplet model and the complement

Fisher's droplet model [24,25] is a physical cluster theory that has successfully described the cluster distributions in percolating systems [40] and lattice gas (Ising) systems [47]; reproduced the compressibility factor at the critical point [48]; predicted (within a few percent) the compressibility factor of real fluids from the triple point to the critical temperature [49,50]; and been used to describe the nucleation rate of real fluids [51,52].

Physical cluster theories of nonideal vapors assume that the monomer-monomer interaction is exhausted in the formation of clusters and that the resulting clusters behave ideally (i.e., they do no interact with each other) [53,54]. Further, clusters of a given number of constituents A_f can be characterized by a chemical potential (per constituent) μ and a partition function $q_{A_f}(T, V)$, which depends on the temperature T and volume V of the fluid and is given by

$$q_{A_f}(T, V) = V \left(\frac{2\pi m_{A_f} T}{h^2} \right)^{\frac{3}{2}} \exp\left(-\frac{\Delta G}{T} \right), \qquad (2)$$

where V is the volume and m_{A_f} is the mass of a fragment of A_f constituents. Here the factor before the exponential is the cube of the fragment's thermal wavelength:

$$\Lambda = \sqrt{\frac{h^2}{2\pi m_{A_f} T}}. \qquad (3)$$

In Eq. (2) ΔG is the free-energy cost for the formation of that cluster [55],

$$\Delta G = \Delta E - T\Delta S + p\Delta V, \qquad (4)$$

where ΔE and ΔS are the energy and entropy cost of the formation of the cluster, respectively, p is the pressure, and ΔV is the change in volume owing to the formation of the cluster.

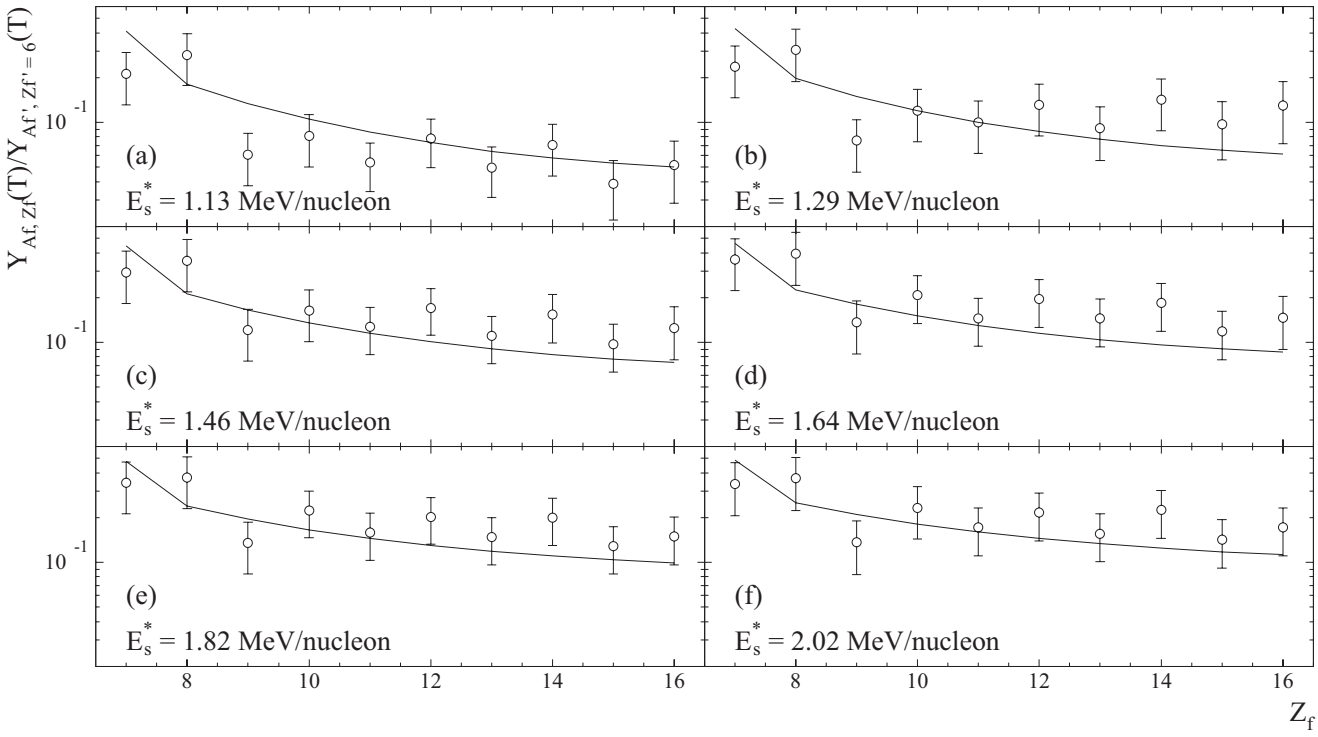

FIG. 4. Fragment yields from the ^{58}Ni+^{12}C $\rightarrow$ ^{70}Se data. Curves show the fit to the data. There are 60 data points fit with three free parameters. The abscissa is a ratio and dimensionless. All data points have error bars, which are not shown when they are smaller than the symbols.

Because of the ideality of the fluid of clusters, the pressure and density are readily determined. The pressure p is

$$p = \frac{T}{V}\sum_{A_f=1}^{\infty} q_{A_f}(T,V)z^{A_f} \tag{5}$$

and the density ρ is

$$\rho = \frac{1}{V}\sum_{A_f=1}^{\infty} A q_{A_f}(T,V)z^{A_f}, \tag{6}$$

where z is the fugacity $z = e^{\mu/T}$. The concentration of size A_f clusters is then

$$\begin{aligned} n_{A_f}(T,z) &= \frac{q_{A_f}(T,V)z^{A_f}}{V} \\ &= z^{A_f}\left(\frac{2\pi m_{A_f}T}{h^2}\right)^{\frac{3}{2}}\exp\left(-\frac{\Delta G}{T}\right) \\ &= q_0\exp\left(\frac{A_f\Delta\mu}{T}\right)\exp\left(-\frac{\Delta G}{T}\right), \end{aligned} \tag{7}$$

where $\Delta\mu$ is a measure of the distance from coexistence in terms of the chemical potential which, following Fisher [24], absorbs the thermal wavelength and q_0 is a normalization constant. At coexistence, $\Delta\mu = 0$, the cluster concentration is given by

$$n_{A_f}(T) = q_0\exp\left(-\frac{\Delta G}{T}\right). \tag{8}$$

There have been many derivations of the form of ΔG, but here we follow a general derivation using the complement method [22] and concentrate on the change in free energy between the initial state and the final state. Because in the complement derivation bulk terms (those terms that are proportional to A) do not survive, they are omitted in the derivation below.

The initial state consists of an equilibrated liquid drop consisting of A_s particles. In the final state the drop has just emitted a cluster or droplet or fragment with A_f particles. Also in the final state along with the fragment is the complement. The complement is what is left of the drop after the fragment has been emitted and thus consists of $A_c = A_s - A_f$ particles. In determining the free energy of the initial and final state, we follow Fisher's contribution to physical cluster theory, which was to endow clusters with a surface energy and to provide an estimate for the entropic part of the free energy associated with the formation of a cluster [24,25].

Because the vapor of clusters is ideal, its internal energy is given by

$$E = \sum_{A=1}^{A=A_s} n_A E_A, \tag{9}$$

where E_A is the binding energy of a cluster and is determined via a liquid drop expansion

$$E_A = a_v A + a_s A^{\sigma}, \tag{10}$$

where a_v is the bulk or volume energy coefficient, a_s is the surface energy coefficient, and σ is an exponent describing

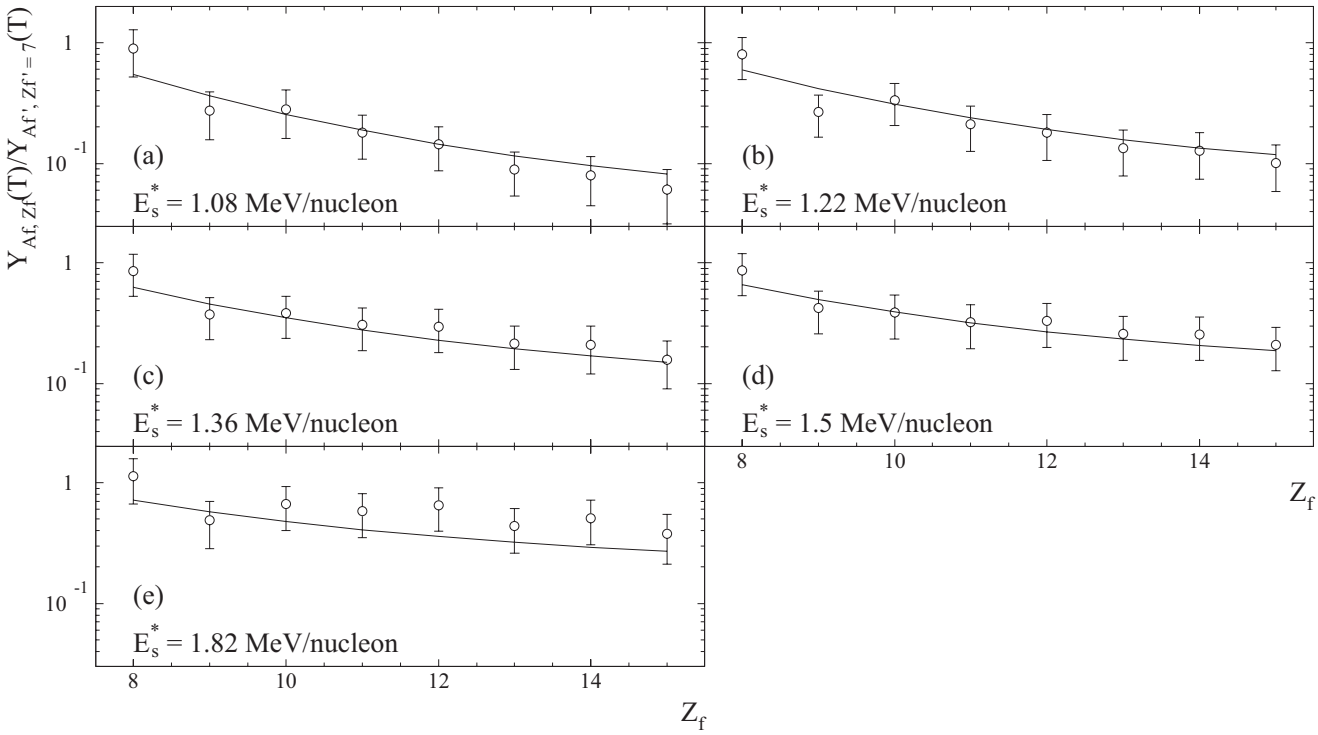

FIG. 5. Fragment yields from the ^{64}Ni+^{12}C $\rightarrow$^{76}Se data. Curves show the fit to the data. There are 40 data points fit with three free parameters. The abscissa is a ratio and dimensionless. All data points have error bars, which are not shown when they are smaller than the symbols.

the relationship between the surface and the volume of the fragment. One expects that $\sigma \approx 2/3$ for three-dimensional systems.

The only contributions to the change in the energy between the final and the initial states are those that are associated with the change in the net surface area. Thus the energy change is given by

$$\Delta E = a_s\left[(A_s - A_f)^\sigma + A_f^\sigma - A_s^\sigma\right]. \tag{11}$$

Similarly, the entropy of the fluid is given by

$$S = \sum_{A=1}^{A=A_s} n_A S_A. \tag{12}$$

Fisher conjectured that the entropy of a cluster could also be estimated with a liquid-drop-type expansion,

$$S_A = b_v A + b_s A^\sigma - \tau \ln A, \tag{13}$$

where b_v is the bulk or volume entropy coefficient and b_s is the surface entropy coefficient. See Ref. [56] for more on the origins of the logarithmic term.

As with the energy, the only contributions to the change in the entropy between the final and the initial states are those associated with the change in the net surface area. Thus the entropic contribution is given by

$$\Delta S = b_s\left[(A_s - A_f)^\sigma + A_f^\sigma - A_s^\sigma\right] - \tau \ln\left[\frac{(A_s - A_f)\,A_f}{A_s}\right]. \tag{14}$$

The contribution to the free energy owing to the change in volume, the $p\Delta V$ term, is negligible compared to the energetic and entropic contributions and is ignored here.

Equations (9) and (12) combine to show that the change in free energy is

$$\Delta G = (a_s - T b_s)\left[(A_s - A_f)^\sigma + A_f^\sigma - A_s^\sigma\right] + T\tau \ln\left[\frac{(A_s - A_f)A_f}{A_s}\right]. \tag{15}$$

At the critical temperature, T_c, the surface's contribution to ΔG vanishes, thus Eq. (15) shows that T_c is

$$T_c = \frac{a_s}{b_s}. \tag{16}$$

Assuming that the coefficients a_s and b_s are independent of the temperature, the quantity $(a_s - T b_s)$ can be rewritten as $a_s\varepsilon$, with

$$\varepsilon = \frac{T_c - T}{T_c}. \tag{17}$$

Now the fragment concentration becomes

$$n_{A_f}(T) = q_0\left[\frac{(A_s - A_f)A_f}{A_s}\right]^\tau \times \exp\left\{-\frac{a_s\varepsilon\left[(A_s - A_f)^\sigma + A_f^\sigma - A_s^\sigma\right]}{T}\right\}. \tag{18}$$

This expression explicitly accounts for all the finite-size effects and thus its parameters are those of the infinite system.

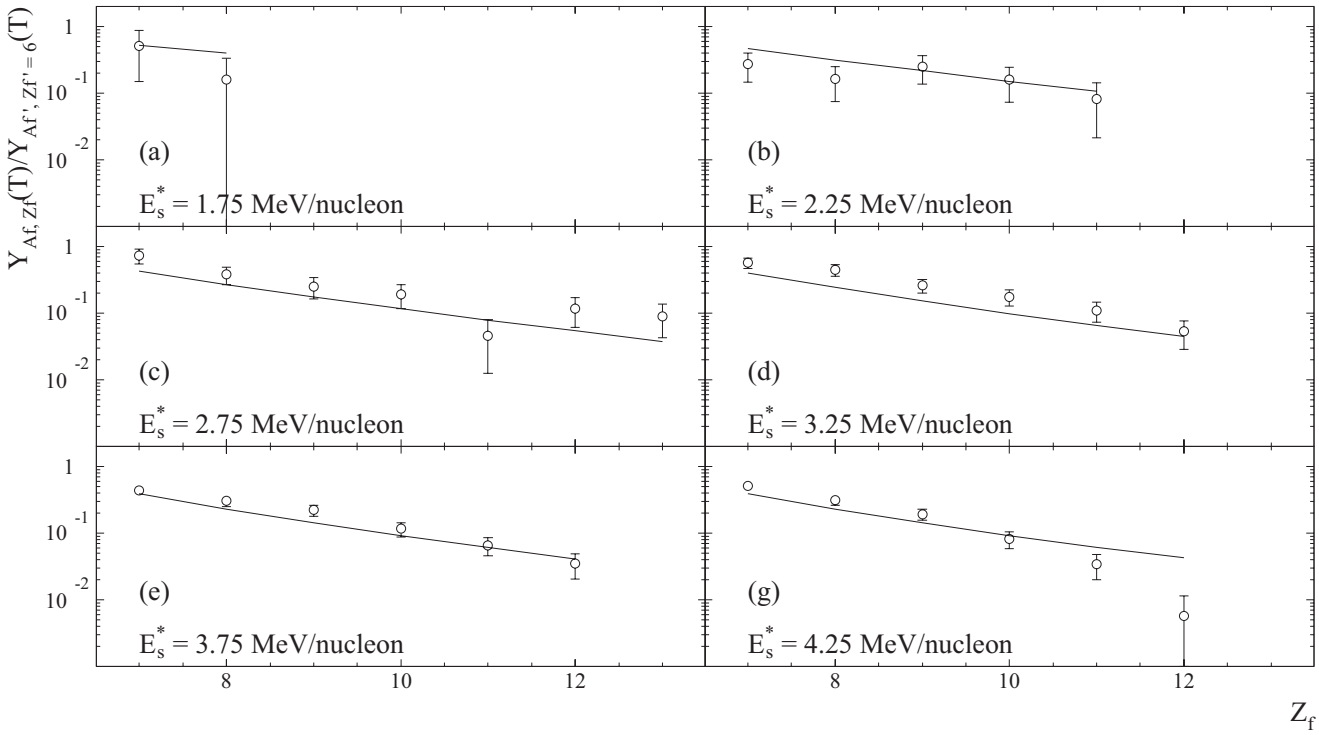

FIG. 6. Fragment yields from the 1 GeV/nucleon ^{84}Kr+^{12}C EOS data. Curves show the fit to the data. There are 32 data points fit with four fit parameters. The abscissa is a ratio and dimensionless. All data points have error bars, which are not shown when they are smaller than the symbols.

This equation was shown to accurately determine the critical temperature of the infinite-system Ising model from cluster distributions of finite-system calculations [22].

In the limit of a bulk liquid where $A_s \to \infty$, then $A_s - A_f \approx A_s$, and we obtain

$$n_{A_f}(T) = q_0 A_f^{-\tau} \exp\left(-\frac{a_s \varepsilon A_f^{\sigma}}{T}\right), \tag{19}$$

which is the expression Fisher derived for the cluster concentration at coexistence [24,25,55].

At the critical point, $\varepsilon = 0$ (the surface free energy vanishes) and the fragment distribution is given by a power law. The power law has been explicitly verified in percolation and Ising systems [6,10,40,47,57–79] and implicitly verified in a wide variety of physical fluids [48,49].

For the present work, the liquid is not infinite and at most $A_s \approx 175$, so Eq. (19) cannot be used. Rather, all the terms in Eq. (18) must be used, in addition to other terms that arise owing to the nuclear nature of the fluid, e.g., a Coulomb term and an isospin term. Those other terms are derived below by examining the initial and final states of the evaporating, equilibrated, excited nuclear source.

B. Characterization of the initial state: Properties of the thermal source

The nucleon number of the excited, equilibrated, evaporating nuclear source is A_s, with Z_s protons and N_s neutrons. For the compound-nucleus experiments, the source is defined as the sum of the target and projectile. For the multifragmentation experiments the source was measured in the experiments and found to be a nucleus smaller in nucleon number than the larger of the projectile or target, as shown in Fig. 1.

The temperature of the thermal source T is not measured directly but is estimated via the Fermi gas model and the measured excitation energy of the thermal source. The excitation energy of the source (in units of MeV/nucleon) is related to the temperature of the source by

$$E_s^* = \frac{1}{k} T^2, \tag{20}$$

where the level density parameter, k, is modified to account for the empirically observed change with excitation energy [80] and is given by [81]

$$k = 8\left[1 + \left(\frac{A_s E_s^*}{E_s^{\text{bind}}}\right)\right]. \tag{21}$$

In Eq. (21) E_s^{bind} is the binding energy of the thermal source. Because the fragment yield distributions analyzed below are measured as a function of the fragment charge (Z_f) and because the fragment mass (A_f) is only estimated, pairing and shell effects are neglected explicitly and the binding energy of a nucleus of nucleon number A (Z protons and N neutrons) is found (in MeV) from the liquid drop expansion [17–19]

$$E_{A,Z}^{\text{bind}} = -a_v(1 - k_v y^2)A + a_s(1 - k_s y^2)A^{\sigma} + \kappa \frac{3}{5}\frac{Z(Z-1)}{r_0 A^{1/3}}, \tag{22}$$

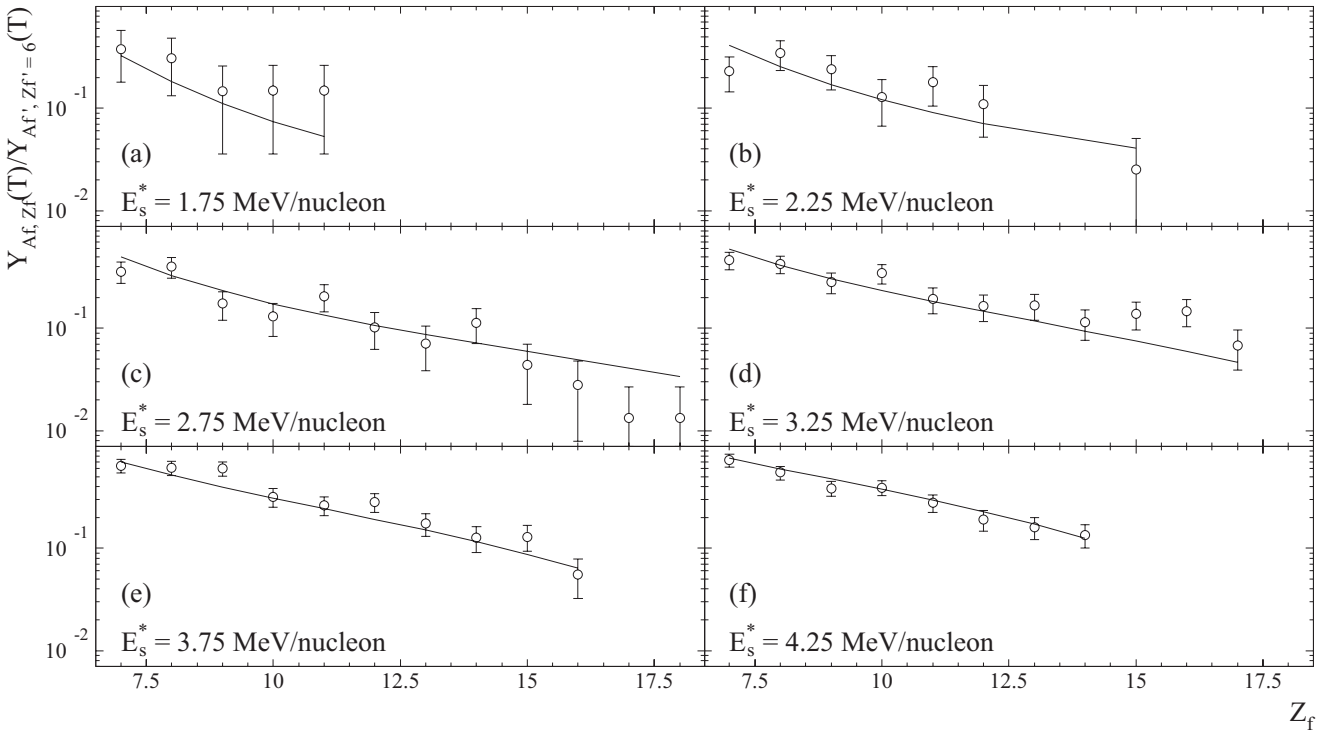

FIG. 7. Fragment yields from the 1 GeV/nucleon ^{139}La+^{12}C EOS data. Curves show the fit to the data. There are 53 data points fit with four free parameters. The abscissa is a ratio and dimensionless. All data points have error bars, which are not shown when they are smaller than the symbols.

where $a_v = 15.7335$, $k_v = 1.6949$, $a_s = 17.8048$, $k_s = 1.0884$, $\kappa = 1.43997$ MeV fm, $r_0 = 1.2181$ fm, and the asymmetry (or isospin) parameter is

$$y = \frac{A - 2Z}{A}. \tag{23}$$

The values of the parameters are taken from Ref. [19] from a fit to the experimental nuclear masses that explicitly neglects pairing and shell effects. Thus the parameter values used here are themselves affected by pairing and shell effects and can then be understood to implicitly account for them. When pairing and shell effects are explicitly taken into account, the above parameters change by 0.5%, 0.9%, 2.6%, 20%, and 0% for a_v, k_v, a_s, k_s, and r_0 respectively. These changes give some indication of the systematic uncertainty that arises from neglecting shell and pairing effects. We note that Eq. (22) already gives us a_s, one of the parameters needed to determine the critical temperature as shown in Eq. (16).

In the case of the compound-nucleus experiments, the angular momentum $\vec{I}$ of the thermal source was estimated [27]. However, we multiplied that estimate by a constant, I_0, which was left as a fitting parameter. For the multifragmentation experiments, we parametrized $\vec{I}$ as

$$|\vec{I}| = |I_0 + I_1 E_s^*|, \tag{24}$$

where the coefficients I_0 and I_1 were left as fit parameters

The energy of the thermal source owing to its angular momentum is (classically)

$$E_s^{\vec{I}} = \frac{|\vec{I}|^2}{\frac{4}{5} m_s r_s^2}. \tag{25}$$

All radii in this work are taken to be

$$r = r_0 A^{1/3}. \tag{26}$$

Following Fisher, the entropy of a nucleus is estimated based on Eq. (13) with σ and τ set to their three-dimensional Ising class values: $\sigma = 0.63946 \pm 0.0008$ and $\tau = 2.209 \pm 0.006$ [40].

The free energy of the thermal source is the free energy of the initial state

$$G_{\text{initial}} = E_s^{\text{bind}} + E_s^{\vec{I}} - T S_s. \tag{27}$$

The pV contribution to the free energy is neglected here.

C. Final state: The fragment and complement

The final state considered here is immediately after the emission (or evaporation) of a neutron, proton, or heavier charged fragment. The fragment has mass m_f, radius r_f, and A_f nucleons (Z_f protons and N_f neutrons).

After fragment emission the thermal source is reduced in nucleon number, is labeled the "complement," and has mass m_c, radius r_c, and A_c nucleons (Z_c protons and N_c neutrons). It is assumed that the the fragment and complement are both

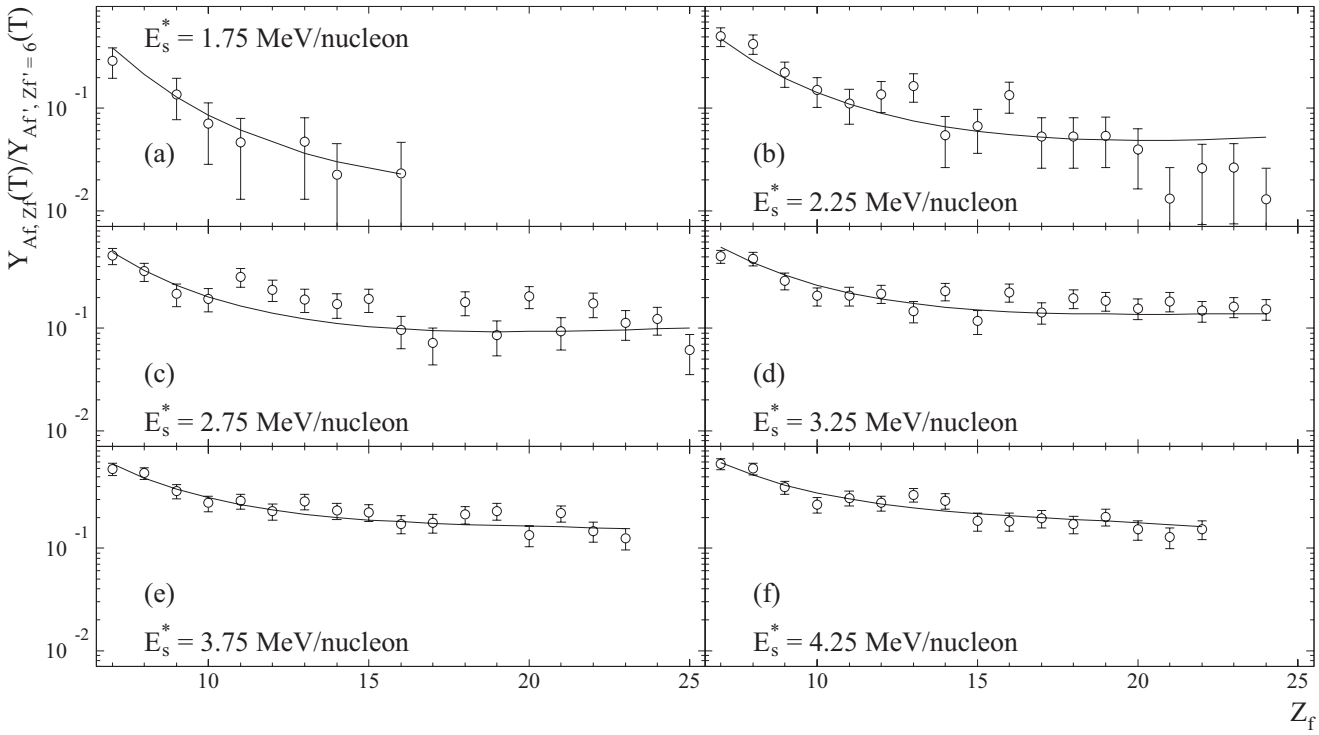

FIG. 8. Fragment yields from the 1 GeV/nucleon ^{179}Au+^{12}C EOS data. Curves show the fit to the data. There are 96 data points fit with four free parameters. The abscissa is a ratio and dimensionless. All data points have error bars, which are not shown when they are smaller than the symbols.

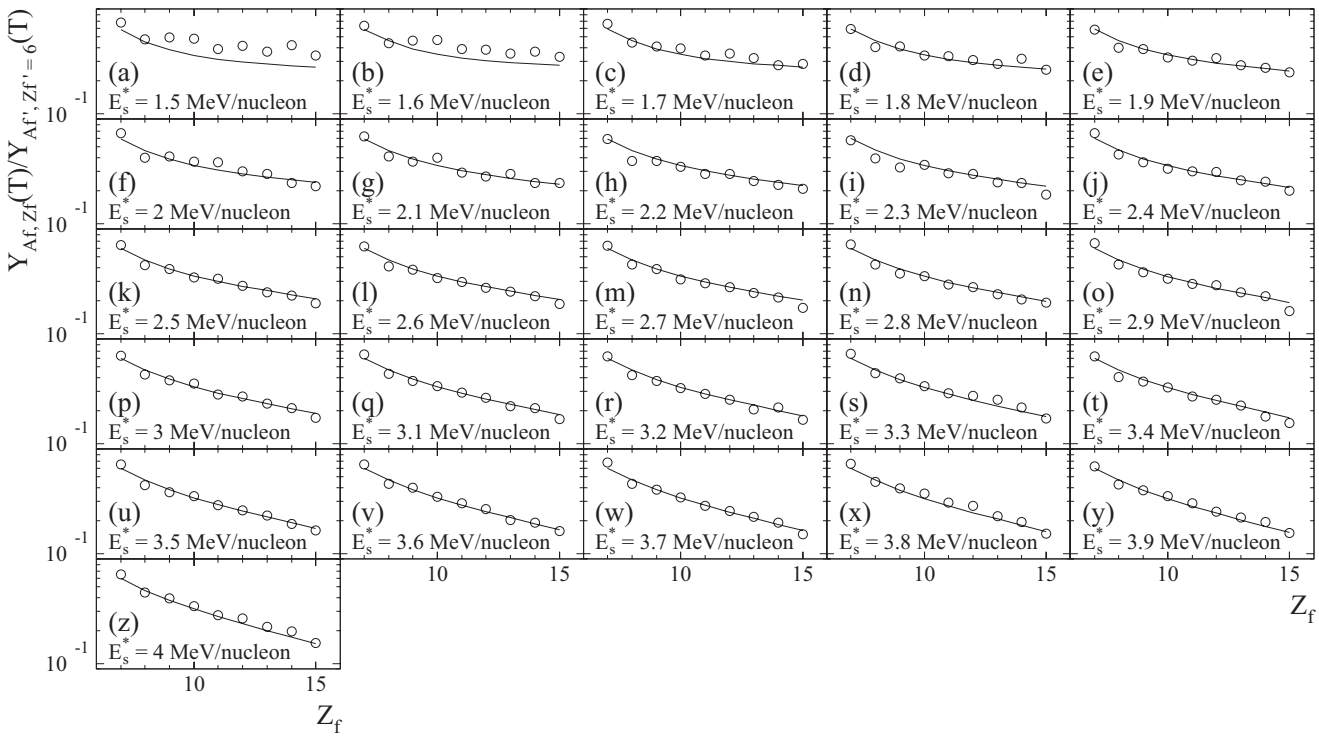

FIG. 9. Fragment yields from the 1 GeV/c $\pi+^{197}$Au ISiS data. Curves show the fit to the data. There are 234 data points fit with four free parameters. The abscissa is a ratio and dimensionless. All data points have error bars, which are not shown when they are smaller than the symbols.

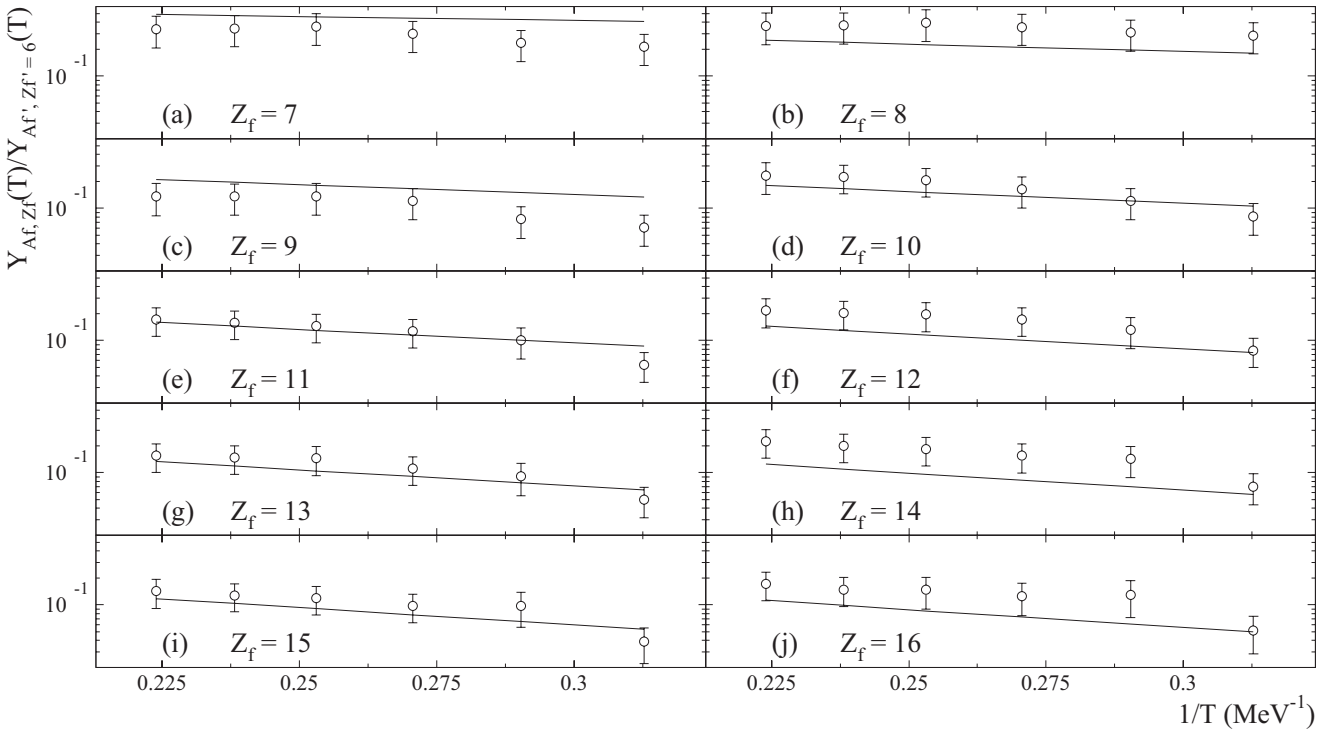

FIG. 10. Arrhenius plots from the ^{58}Ni+^{12}C $\rightarrow^{70}$Se data. Curves show the fit to the data. There are 60 data points fit with three free parameters. The abscissa is a ratio and dimensionless. All data points have error bars, which are not shown when they are smaller than the symbols.

spherical, at normal nuclear density, and that the surface of the fragment and the surface of the complement are in contact.

Conservation of angular momentum dictates that the fragment and complement system have the same angular momentum as the thermal source. The energy associated with this angular momentum is then (classically)

$$E^{\vec{I}}_{\mathrm{f+c}} = \frac{|\vec{I}|^2}{\frac{4}{5}\left(m_c r_c^2 + m_f r_f^2\right) + 2\frac{m_c m_f}{m_c+m_f}(r_c + r_f)^2}. \tag{28}$$

The Coulomb energy between the fragment and the complement is

$$E^{\mathrm{Coulomb}}_{\mathrm{f+c}} = \kappa \frac{Z_f Z_c}{r_f + r_c}. \tag{29}$$

The free energy of the final state is

$$G_{\mathrm{final}} = E^{\mathrm{bind}}_{\mathrm{f}} + E^{\mathrm{bind}}_{\mathrm{c}} + E^{\vec{I}}_{\mathrm{f+c}} + E^{\mathrm{Coulomb}}_{\mathrm{f+c}} - T(S_f + S_c). \tag{30}$$

The determination of quantities associated with the fragment and complement are discussed below.

1. *Properties of the fragment*

The charge of the fragment Z_f is measured by the detectors in the experiments. The nucleon number of the observed fragment A^{obs}_f is estimated via the EPAX parametrization [82],

$$A^{\mathrm{obs}}_f = -0.10167 + 1.9638 Z_f + 0.0057221 Z_f^2. \tag{31}$$

The excitation energy of the fragment (in MeV) is estimated with the Fermi gas relation,

$$E^*_f = \frac{1}{k} A_f T^2 = \frac{1}{k}\left(A^{\mathrm{obs}}_f + N_{\mathrm{evap}}\right) T^2, \tag{32}$$

where A_f is the nucleon number of the fragment prior to any secondary decay or evaporation (under the approximation that only neutrons are evaporated from the fragments).

The number of neutrons N_{evap} that can be evaporated from a nucleus (A^{obs}_f, Z_f) is approximately

$$N_{\mathrm{evap}} \approx \frac{E^*_f}{B_n + 2T}, \tag{33}$$

where B_n is the neutron binding energy of the nucleus in question. This is estimated as

$$B_n \approx m_{A^{\mathrm{obs}}_f - 1, Z_f} + m_n - m_{A^{\mathrm{obs}}_f, Z_f} \approx E^{\mathrm{bind}}_{A^{\mathrm{obs}}_f - 1, Z_f} - E^{\mathrm{bind}}_{A^{\mathrm{obs}}_f, Z_f}. \tag{34}$$

Combining Eqs. (32) and (33) gives

$$N_{\mathrm{evap}} \approx d_2 \left(\frac{\frac{1}{k} T^2 A^{\mathrm{obs}}_f}{B_n + 2T - \frac{1}{k} T^2} \right), \tag{35}$$

where d_2 is a fit parameter to account for the crude nature of this approximation.

The fragment's initial nucleon number A_f is

$$A_f = A^{\mathrm{obs}}_f + N_{\mathrm{evap}}. \tag{36}$$

As mentioned above, this estimate assumes that only neutrons are emitted during the secondary decay. The fragment's

binding energy (E_f^{bind}), radius (r_f), and entropy (S_f) are determined using Eqs. (22), (23), and (13), respectively, with A_f and Z_f.

2. *Properties of the complement*

Conservation of mass and charge give the mass A_c, charge Z_c, and neutron number N_c of the complement. The binding energy (E_c^{bind}), radius (r_c), and entropy (S_c) of the complement are determined using Eqs. (22), (23), and (13), respectively, with A_c and Z_c.

D. Average fragment yields

All of the experiments discussed here measure the average yield of fragments with a given charge as a function of the excitation energy of the thermal source $Y_{Z_f}(E_s^*)$, where

$$Y_{Z_f}(E_s^*) = \frac{\text{number of } Z_f \text{ fragments in events with } E_s^*}{\text{total number of events with } E_s^*},$$

and its associated error in the mean $\delta Y_{Z_f}(E_s^*)$.

It is assumed that there is a one-to-one relationship between the excitation energy of the thermal source and the temperature and a one-to-one relationship between the charge of a fragment and its nucleon number. Thus the fragment charge yields as a function of the excitation energy are equivalent to the fragment mass yields as a function of temperature, which is written $Y_{A_f,Z_f}(T)$.

For the first fragments emitted their yield is given by

$$Y_{A_f,Z_f}(T) = \Delta t\, R_{A_f,Z_f}(T) = Y, \tag{37}$$

where Δt is the time duration of the measurement of the decay of the thermal source and $R_{A_f,Z_f}(T)$ is the rate of fragment emission.

Equation (1) shows that the fragment emission rate from the thermal source is related to the concentration $n_{A_f,Z_f}(T)$ of any species (A_f, Z_f,) in the "virtual" vapor which matches the evaporation (or emission) flux out of the thermal source with the condensation flux into the thermal source [21]:

$$R_{A_f,Z_f}(T) \approx \langle v_{A_f}\sigma_{inv}\rangle n_{A_f,Z_f}(T). \tag{38}$$

The mean thermal velocity of the fragment normal to the plane of emission is given as

$$\langle v_{A_f}\rangle = \sqrt{\frac{T}{2\pi m_{A_f}}}, \tag{39}$$

where an ideal vapor has been assumed. The inverse cross section for fragment emission is

$$\sigma_{inv} = 4\pi(r_f + r_c)^2, \tag{40}$$

where only the geometric cross section is considered, as the Coulomb effects are explicitly dealt with below [23].

Equation (8) shows that the concentration of the virtual vapor depends on the free-energy cost of cluster formation ΔG. For a fragment emitted from an excited nucleus, ΔG is given by Eqs. (27) and (30) and is

$$\Delta G = E_f^{bind} + E_c^{bind} + E_{f+c}^{\vec{I}} + E_{f+c}^{Coulomb} - E_s^{bind} - E_s^{\vec{I}} - T\left\{b_s\left(A_f^\sigma + A_c^\sigma - A_s^\sigma\right) - \tau \ln\left(\frac{A_f A_c}{A_s}\right)\right\}. \tag{41}$$

This can be simplified and written as

$$\Delta G = G_{final} - G_{initial} = a_s A_f^\sigma - T\left(b_s A_f^\sigma - \tau \ln A_f\right) + \Delta\mu_{nfs} = \Delta G_\infty + \Delta\mu_{nfs}, \tag{42}$$

where $\Delta\mu_{nfs}$ absorbs all the terms in Eq. (41) (and is divided by A_f) not explicitly written in Eq. (42). $\Delta\mu_{nfs}$ is an "effective chemical potential" that arises owing to the nuclear nature and finite size of the thermal source. The factors not absorbed in $\Delta\mu_{nfs}$ describe the free-energy cost of the formation of a fragment from the bulk nuclear matter, which is written as ΔG_∞.

E. Fitting the experimental charge yields

The fragment charge yields are given by

$$Y_{A_f,Z_f}(T) = \Delta t\,\langle v_f\sigma_{inv}\rangle q_0 \exp\left(-\frac{\Delta G}{T}\right) = \Delta t\,\langle v_f\sigma_{inv}\rangle \exp\left(-\frac{\Delta\mu_{nfs}}{T}\right) \times q_0 A_f^{-\tau} \exp\left(-\frac{a_s A_f^\sigma \varepsilon}{T},\right) \tag{43}$$

a formula that depends on several unknown quantities, e.g., Δt and q_0. However, the ratio of the yield of a fragment of a given charge at a given excitation energy $Y_{A_f,Z_f}(T)$ to some reference yield of a fragment with another charge at the same excitation energy $Y_{A_f',Z_f'}(T)$ cancels all the constants of proportionality and several unknown quantities. Therefore, the ratio of charge yields was fitted with the reference yield taken as the yield of fragments with the charge equal to the lower limit of the Z_f fit range listed in Table I. The ratio of the charge yields is given by

$$\frac{Y_{A_f,Z_f}(T)}{Y_{A_f',Z_f'}(T)} = \frac{\langle v_f\sigma_{inv}\rangle}{\langle v_f'\sigma_{inv}'\rangle} \exp\left(\frac{\Delta\mu_{nfs}' - \Delta\mu_{nfs}}{T}\right) \times \exp\left(\frac{\Delta G_\infty'}{T}\right) A_f^{-\tau} \exp\left(-\frac{a A_f^\sigma \varepsilon}{T}\right) = \Theta A_f^{-\tau} \exp\left(-\frac{a_s A_f^\sigma \varepsilon}{T}\right), \tag{44}$$

TABLE I. Fit details.

Reaction	No. of points fit	No. of parameters	Z_f range	E_s^* range (MeV/nucleon)
^{58}Ni+^{12}C $\rightarrow ^{70}$Se	60	3	[6, 16]	[1.13, 2.02]
^{64}Ni+^{12}C $\rightarrow ^{76}$Se	40	3	[7, 15]	[1.08, 1.82]
^{84}Kr+^{12}C	32	4	[6, 13]	[1.75, 4.75]
^{139}La+^{12}C	53	4	[6, 18]	[1.75, 4.75]
^{197}Au+^{12}C	96	4	[6, 25]	[1.75, 4.75]
π+^{197}Au	234	4	[6, 15]	[1.50, 4.00]

where Θ absorbs all factors other than those in Fisher's model for the bulk fluid. The only free parameters in Eq. (44) are d_2, the secondary decay coefficient; I_0 (and I_1 for the multifragmentation data), the angular momentum parameter(s); and b_s, the surface entropy coefficient. For most of the fragments considered here, secondary decay results in the evaporation of three or fewer neutrons.

Previous attempts similar to the fitting of data suggested by Eq. (44) have been made. Reference [3] fit inclusive fragment yields with a form of Fisher's model that used the liquid drop model to parametrize the energy cost of fragment formation. However, that work did not account for finite-size effects, the fragment-complement Coulomb energy or the effects of angular momentum. In Refs. [11] and [40] the multifragmentation data presented here were fit with a version of Fisher's model that included an ad hoc Coulomb energy parametrization but did not account for the effects of finite size or angular momentum. In Ref. [21] some of the compound-nucleus reaction data presented here were fit with Fisher's model where all the effects of finite size, Coulomb energy, and angular momentum were absorbed into a chemical potential, which yielded much less physical insight than the present analysis.

Table I lists the fragment charge and excitation energy range over which the fits were performed. The lower limit in the fit range of Z_f for the reactions ^{64}Ni+^{12}C $\rightarrow$^{76}Se was set by the available data, while for the other data sets it was for fragments sufficiently large to ensure that they were emitted first, or not at all. The upper limit in the fit range of Z_f for the reactions ^{58}Ni+^{12}C $\rightarrow$^{70}Se and π+^{197}Au is determined by the available data, while for the other data sets it is determined by the largest fragment for which the fragment-complement scheme is appropriate, i.e., $Z_f < Z_s/2$, or the largest value of Z_f present in the data, whichever is smaller. The range in excitation energy is determined by starting at excitation-energy values where shell effects cease and where there are one or fewer fragments in the Z_f fit range. Coupling Table I and Eqs. (20) and (21) shows that the range in temperature considered by the analysis in this paper is 2.75 MeV $\leqslant T \leqslant$ 7.2 MeV.

TABLE II. Fitting results. Based on these results the critical temperature of bulk nuclear matter is $T_c = 17.9 \pm 0.4$ MeV. The average χ^2_ν is 1.8, with a root mean square deviation of 1.1.

Reaction	χ^2_ν	d_2	b_s	T_c (MeV)
^{58}Ni+^{12}C $\rightarrow$^{70}Se	1.3	0.1 ± 0.1	0.97 ± 0.02	18.4 ± 0.3
^{64}Ni+^{12}C $\rightarrow$^{76}Se	0.4	0.5 ± 0.2	0.99 ± 0.01	18.0 ± 0.2
^{84}Kr+^{12}C	3.3	$0.0 \pm 5 \times 10^{-5}$	1.02 ± 0.01	17.5 ± 0.2
^{139}La+^{12}C	1.1	1.8 ± 0.1	0.973 ± 0.008	18.3 ± 0.2
^{197}Au+^{12}C	1.3	1.1 ± 0.1	1.007 ± 0.007	17.7 ± 0.1
π+^{197}Au	3.2	$0.0 \pm 3 \times 10^{-4}$	1.032 ± 0.001	17.26 ± 0.02

For the compound-nucleus data, there are three fit parameters for each data set: b, d_2, and I_0. For the multifragmentation data, there are four fit parameters for each data set: b, d_2, I_0, and I_1. On average, there are ~23 points per fit parameter.

The results for b and d_2 are listed in Table II. Figure 2 shows the results for the critical temperature of the bulk nuclear matter determined from these experiments as a function of the mass of the thermal source. The multiple points shown in

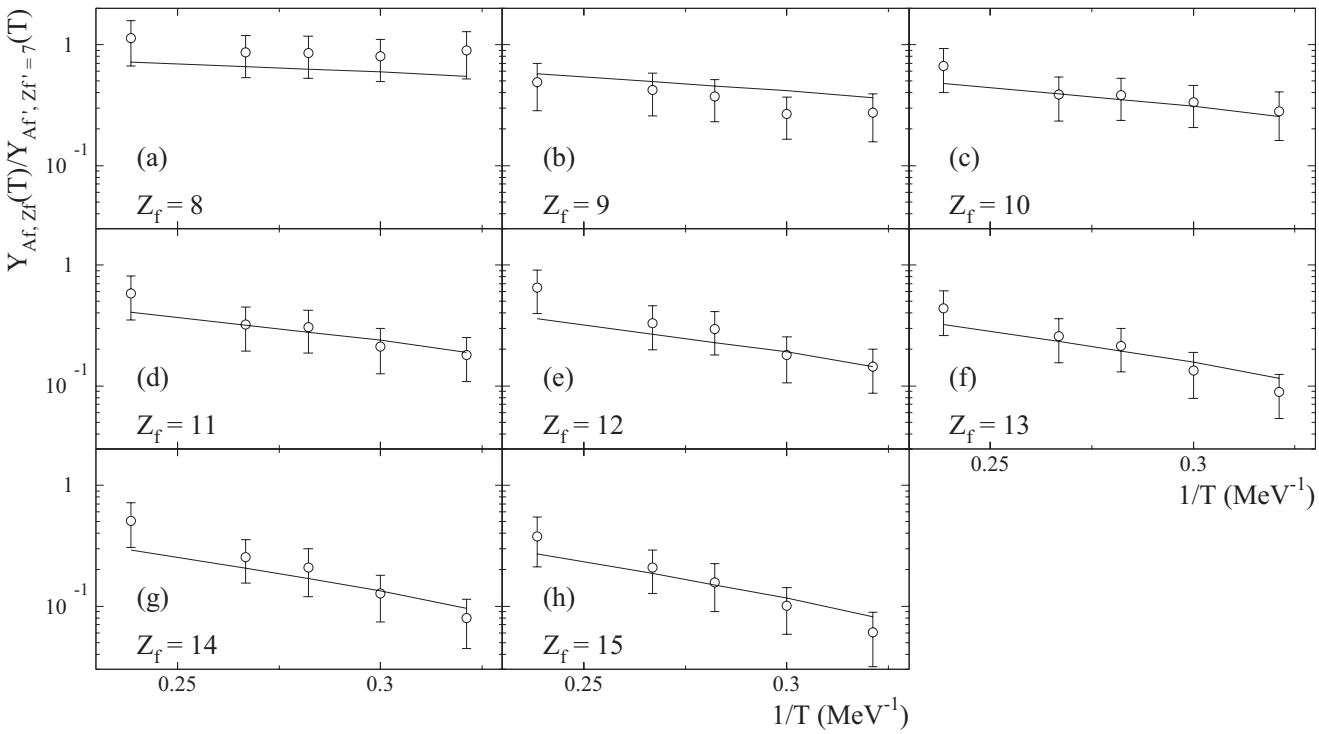

FIG. 11. Arrhenius plots from the ^{64}Ni+^{12}C $\rightarrow$^{76}Se data. Curves show the fit to the data. There are 40 data points fit with three free parameters. The abscissa is a ratio and dimensionless. All data points have error bars, which are not shown when they are smaller than the symbols.

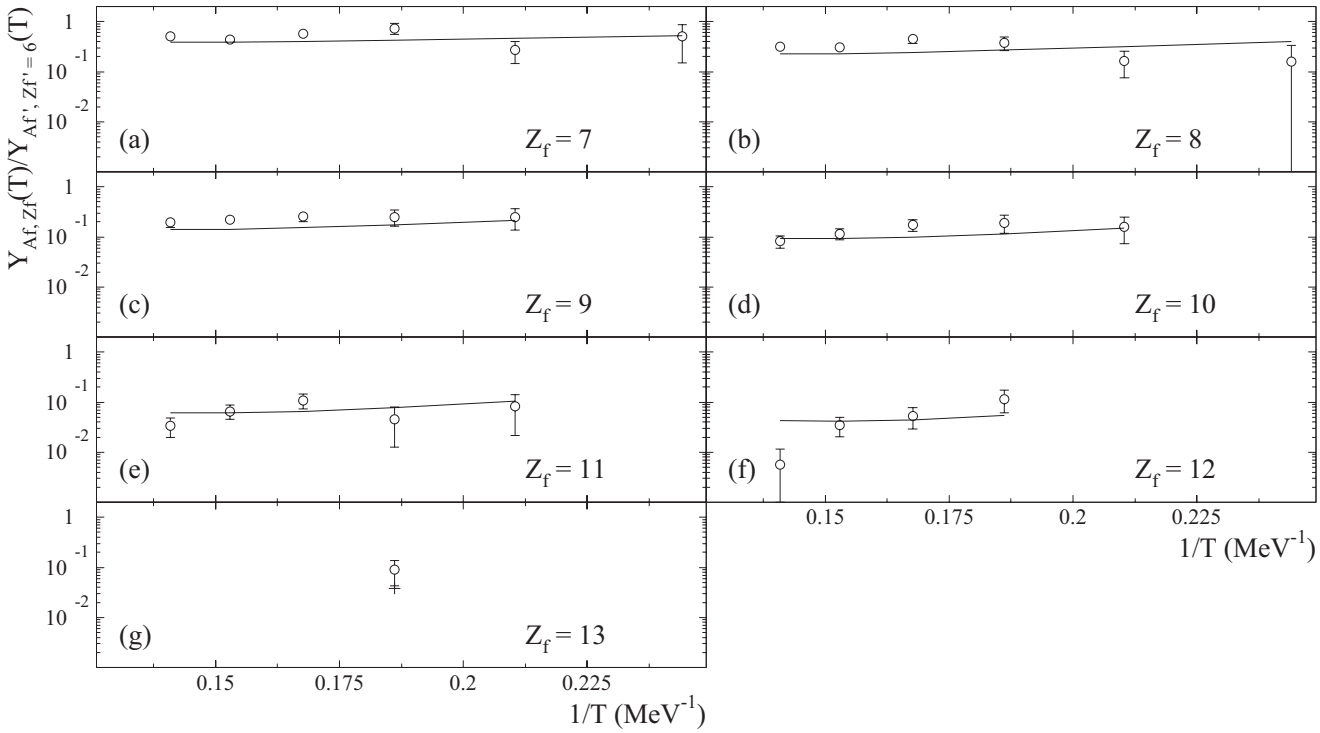

FIG. 12. Arrhenius plots from the 1 GeV/nucleon ^{84}Kr+^{12}C data. Curves show the fit to the data. There are 32 data points fit with four free parameters. The abscissa is a ratio and dimensionless. All data points have error bars, which are not shown when they are smaller than the symbols.

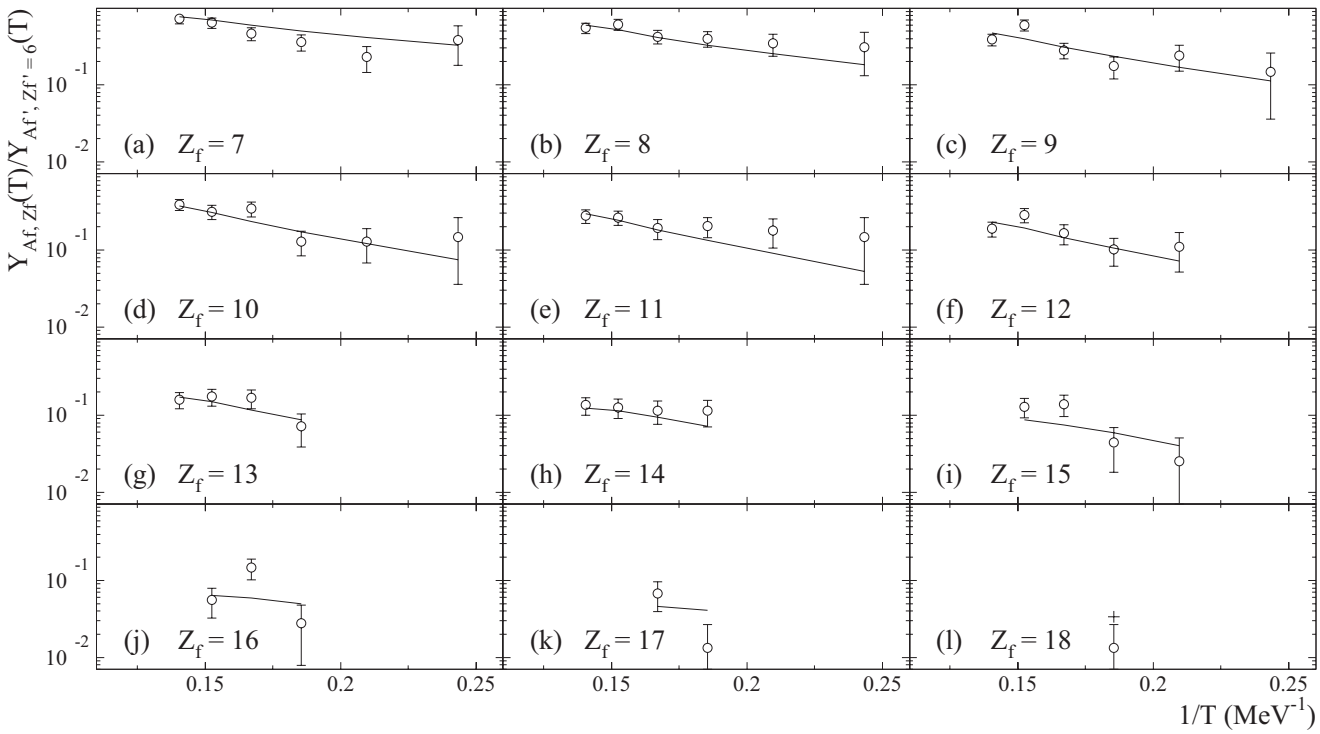

FIG. 13. Arrhenius plots from the 1 GeV/nucleon ^{139}La+^{12}C data. Curves show the fit to the data. There are 53 data points fit with four free parameters. The abscissa is a ratio and dimensionless. All data points have error bars, which are not shown when they are smaller than the symbols.

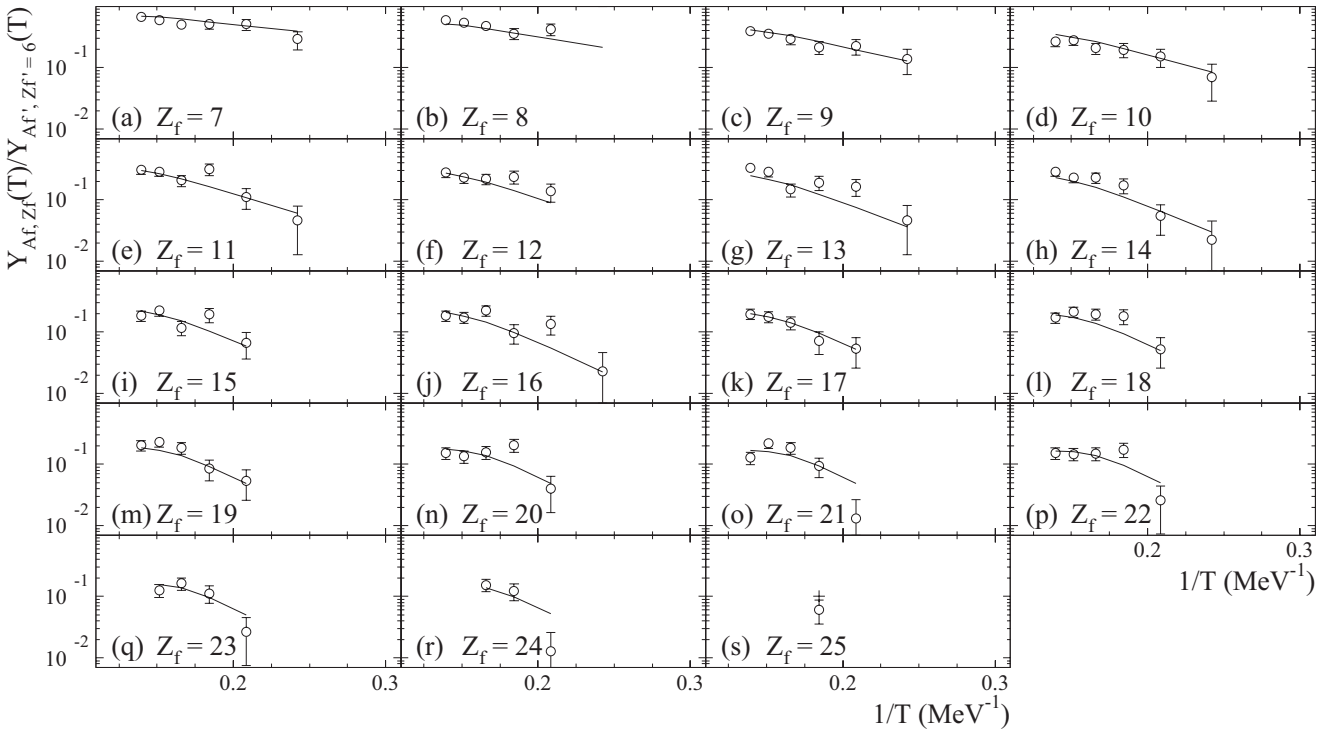

FIG. 14. Arrhenius plots from the 1 GeV/nucleon ^{179}Au+^{12}C data. Curves show the fit to the data. There are 96 data points fit with four free parameters. The abscissa is a ratio and dimensionless. All data points have error bars, which are not shown when they are smaller than the symbols.

Fig. 2 for the EOS and ISiS experiments are caused by the differing mass and charge of the excited thermal sources; the masses and charges of the excited thermal sources are shown in Fig. 1.

Figure 3 shows the result for the angular momentum from the fits. Also shown in that figure is an estimate of the angular momentum that is thermal in nature and is based on the angular momentum that would be imparted by the evaporation of a source beginning with $\vec{I} = 0$ [83]. This estimate serves as a lower limit on the estimate of the angular momentum. The results for the angular momentum from the fits to the compound-nucleus data and the EOS multifragmentation data are of the same order of magnitude of the thermal estimate. However, the results for the angular momentum from the fits of the ISiS data are approximately three times the thermal estimate. It is not clear why the ISiS data indicate such a large angular momentum, however, that is the only experiment with a lighter projectile and a heavier target.

The results of the surface entropy coefficient b_s from all the experiments agree to within 3%. Combining this estimate of b_s with the value of a_s [given below Eq. (22)] gives an estimate of the critical temperature of the bulk nuclear matter as $T_c = 17.9 \pm 0.4$ MeV via Eq. (16). This value is the result of averaging the results of our analysis applied to all six different reactions. The error quoted here is the root mean square (RMS) variation of those values. That error then gives some estimate of the systematic uncertainties of our analysis.

We note that because of the use of the complement correction [22], and because of the effects of Coulomb, isospin, angular momentum, etc., the value of T_c given above is the critical temperature of infinite bulk nuclear matter. The complement correction has accounted for the effects of finite size. Another type of analysis of other multifragmentation data using a different method of accounting for finite-size effects leads to an estimate of T_c that is within 10% of the value given in this work [84].

The value of T_c given above agrees with some theoretical predictions [85–91]. There is more discussion, with comparison to theory, below. Figure 2 shows the value of T_c as a function of the mass of the thermal sources in the experiments.

Figures 4 through 9 show the fragment charge yield ratios as a function of the fragment charge. Figures 10 through 15 show Arrhenius plots in the form of the fragment charge yield ratios as a function of the inverse temperature. In all these figures, the data are shown by open circles with error bars and the fits are shown by solid lines. Solid lines are segments drawn (to guide the eye) between the fit values at each Z_f or $1/T$. In the plots shown in Figs. 4 through 16 all of the data (all fragments of all charges and all excitation energies) for a given experiment were fit simultaneously.

Alternatively, one can combine the results for a given data set shown in Figs. 4 through 15 by plotting $Y_{A_f,Z_f}(T)/Y_{A'_f,Z'_f}(T)$ divided by $\Theta A_f^{-\tau}$ as a function of $aA^{\sigma}\varepsilon/T$, also called a "Fisher plot." This collapses all the measured fragment yield ratios for any A_f, Z_f, and E_s^* onto a single curve. This is shown for all the data sets in Fig. 16.

Figures 16(a)–16(f) show the fragment yields from the (a) ^{64}Ni+^{12}C $\rightarrow$ ^{76}Se data (40 data points fit with three free parameters); (b) ^{58}Ni+^{12}C $\rightarrow$ ^{70}Se data (60 data points fit with three free parameters); (c) 1 GeV/c π+^{197}Au ISiS data (234 data points fit with four free parameters); (d) 1 GeV/nucleon ^{179}Au+^{12}C EOS data (96 data points fit with

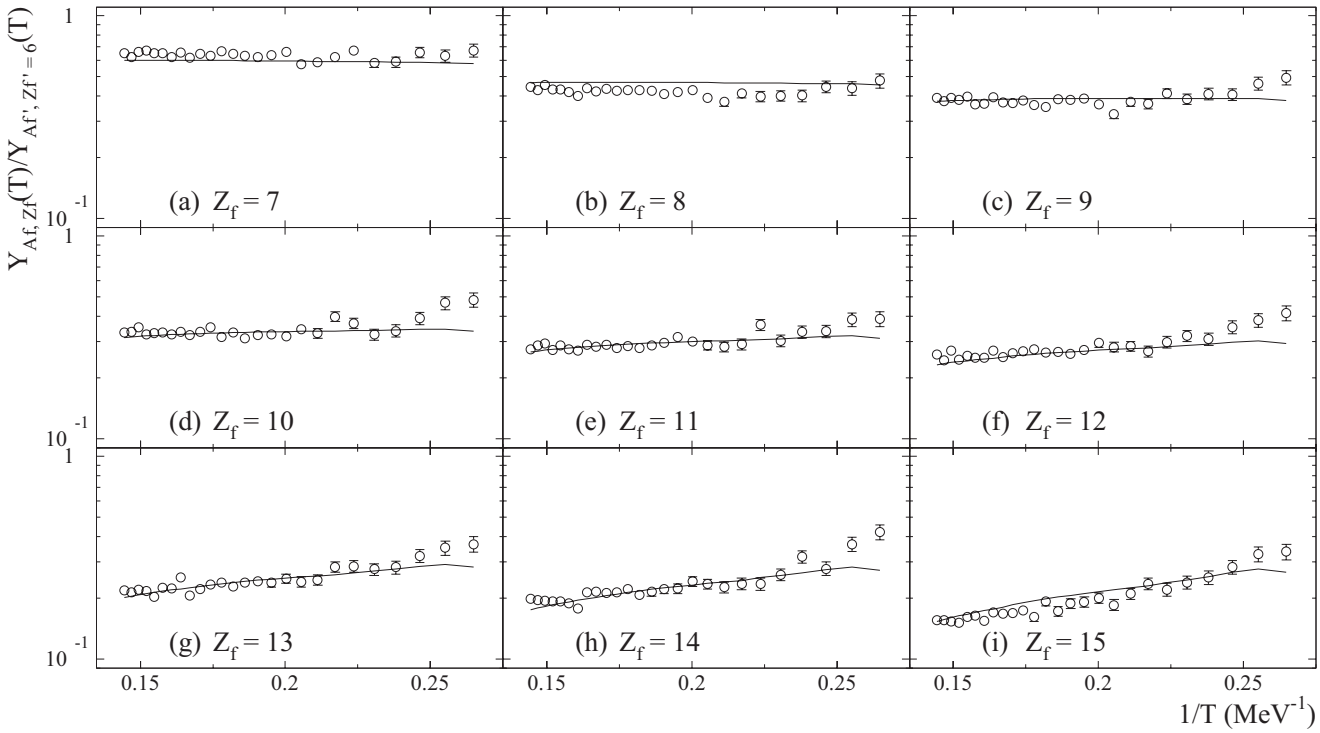

FIG. 15. Arrhenius plots from the 1 GeV/c $\pi+^{197}$Au data. Curves show the fit to the data. There are 234 data points fit with four free parameters. The abscissa is a ratio and dimensionless. All data points have error bars, which are not shown when they are smaller than the symbols.

four free parameters); (e) 1 GeV/nucleon ^{139}La+^{12}C EOS data (53 data points fit with four free parameters.); and (f) 1 GeV/nucleon ^{84}Kr+^{12}C EOS data (32 data points fit with four fit parameters). In total, 515 data points were fit with just 22 free parameters, nearly 23 data points per free parameter. The number of free parameters could be reduced further, to 17, by using a common parameter for b_s for all the data sets (Table II shows that the value of b_s varies less than 3% between data sets).

Because the finite-size effects, Coulomb effects, etc., have been scaled away (by dividing the yield ratios by Θ), the plots in Fig. 16 show the coexistence curve of bulk nuclear matter in terms of the concentration of droplets of the bulk nuclear fluid that would comprise a saturated vapor in equilibrium with an infinite, bulk nuclear liquid.

F. Systematic errors

In order to make some estimate of the systematic errors the analysis above was repeated two more times. One of these analyses removed the energy dependence of the level density parameter in Eq. (21) so that $k = 8$ is constant. The critical temperature resulting from those fits was 16.5 ± 0.7 MeV, with the average $\chi^2_\nu = 1.6$ and an RMS deviation of 1.0.

The other of these analyses removed any secondary decay by fixing $d_2 = 0$. The critical temperature resulting from those fits was 15.0 ± 0.3 MeV, with the average $\chi^2_\nu = 1.9$ and an RMS deviation of 1.0. The result of these analyses suggests that the systematic error associated with the estimate of the critical temperature of bulk nuclear matter measured here is approximately 3 MeV.

V. CONSTRUCTING THE PHASE DIAGRAM

Fitting of the data as illustrated above gave the critical temperature of the bulk nuclear matter. Once T_c is determined, it is possible to determine the entire coexistence curve of the bulk nuclear matter which completely maps the liquid-vapor phase diagram.

The first step is to determine the coexistence curve in reduced units:

$$\frac{p}{p_c}, \quad \frac{\rho}{\rho_c}, \quad \text{and} \quad \frac{T}{T_c}. \tag{45}$$

where p is the pressure, ρ is the density, and the subscript "c" denotes values of the quantities at the critical point.

It is assumed that the formation of fragments exhausts all nonidealities, so that the pressure and density can be obtained by simple sums. The pressure is

$$p = T \sum_A n_A(T) = T \sum_A q_0 A^{-\tau} \exp\left(-\frac{a_s A^\sigma \varepsilon}{T}\right), \tag{46}$$

and at the critical point

$$p_c = T_c \sum_A n_A(T_c) = T_c q_0 \sum_A A^{-\tau}. \tag{47}$$

The density is given by

$$\rho = \sum_A A n_A(T) = \sum_A q_0 A^{1-\tau} \exp\left(-\frac{a_s A^\sigma \varepsilon}{T}\right), \tag{48}$$

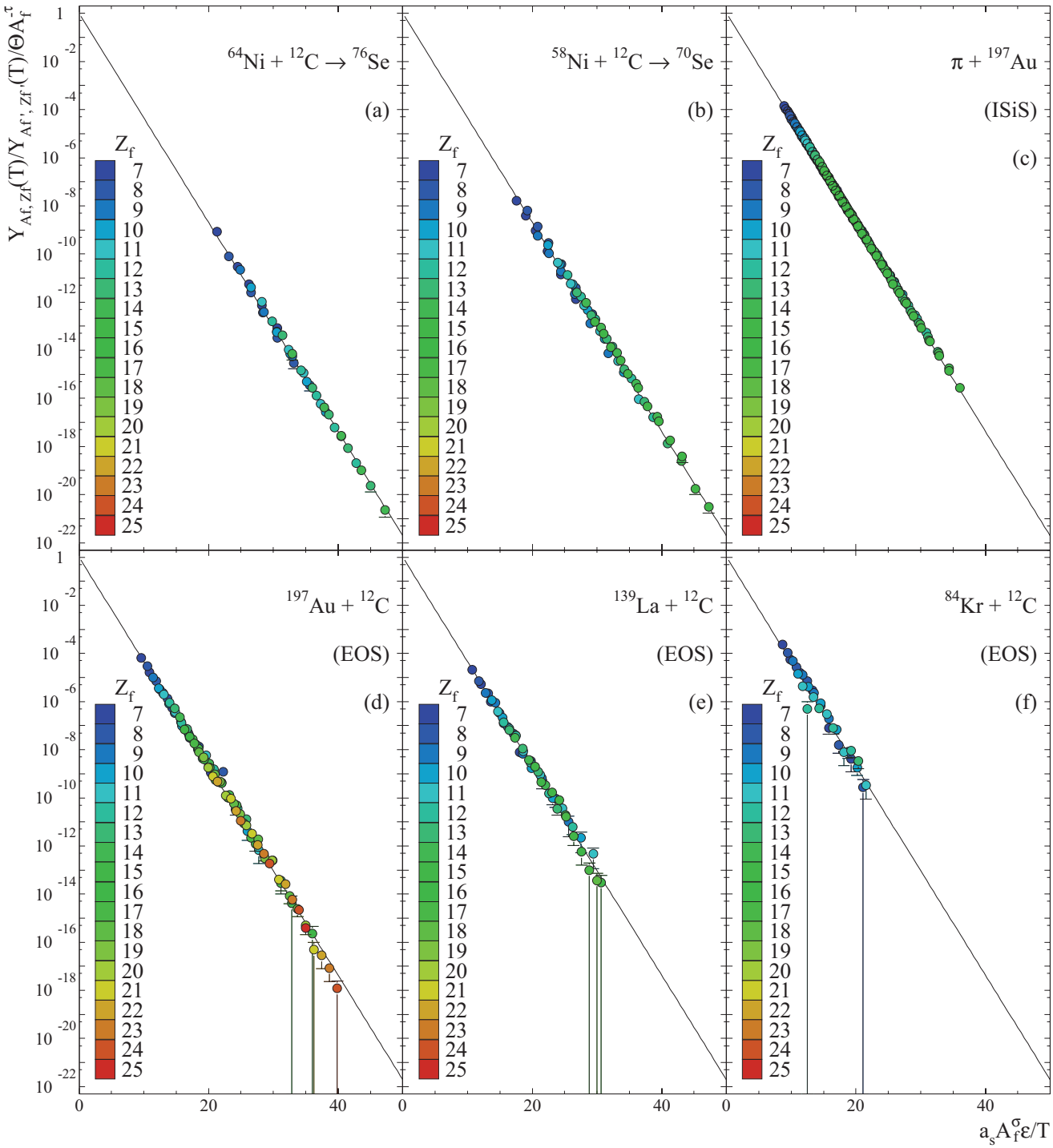

FIG. 16. (Color online) Scaled charge yields for all six reactions, also called "Fisher plots." Solid lines show the fits to the data. All data points have error bars, which are not shown when they are smaller than the symbols. Both axes show ratios that are dimensionless. The charge of a fragment is given by the color (online) of the point as indicated by the color (online) scale. Plots show the scaled fragment yields from the (a) ^{64}Ni+^{12}C $\rightarrow$^{76}Se data; (b) ^{58}Ni+^{12}C $\rightarrow$^{70}Se data; (c) 1 GeV/c π+^{197}Au ISiS data; (d) 1 GeV/nucleon ^{179}Au+^{12}C EOS data; (e) 1 GeV/nucleon ^{139}La+^{12}C EOS data; and (f) 1 GeV/nucleon ^{84}Kr+^{12}C EOS data. Not all plots have a fragment with every charge between $Z_f = 7$ and $Z_f = 25$. See Table I for the fragment charge range for all data sets. There is further discussion in the text.

and at the critical point

$$\rho_c = \sum_A A n_A(T_c) = q_0 \sum_A A^{1-\tau}. \qquad (49)$$

Using the reduced quantities removes the unknown normalization q_0. All other quantities in the above sums are known. The errors associated with T_c, τ, and σ are propagated to generate errors in the reduced quantities.

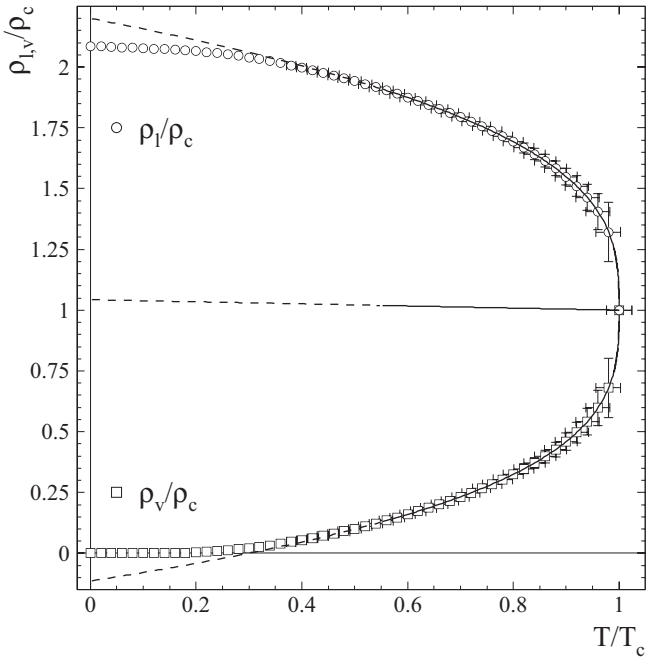

FIG. 17. Reduced density-reduced temperature coexistence curve for bulk nuclear matter. Open squares show the vapor branch. Open circles show the liquid branch. Solid curves show the results of the fit to the vapor branch. Dashed curves show the extrapolation of that fit. The dashed line shows the extrapolation of the law of rectilinear diameter. Both axes show ratios and are dimensionless. See text for details.

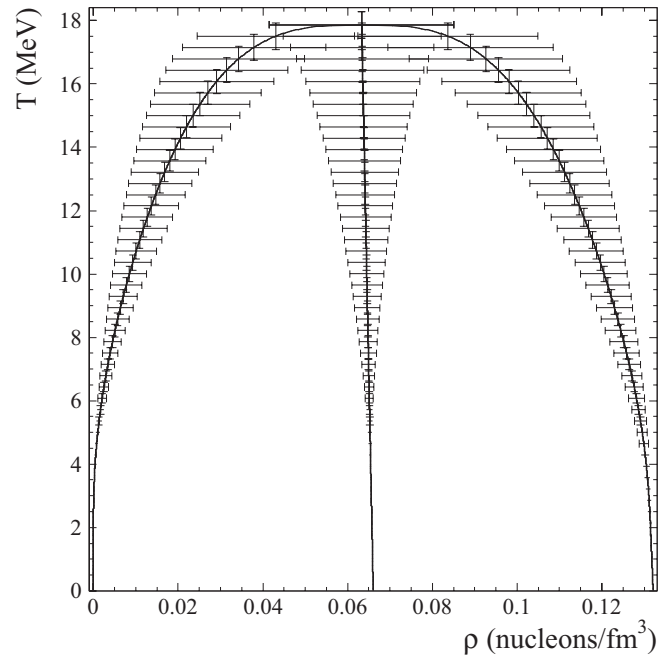

FIG. 18. Temperature-density coexistence curve for bulk nuclear matter. Errors are shown for selected points to give an idea of the error in the entire coexistence curve.

A. Reduced density

The open squares in Fig. 17 show the vapor branch of the ρ-T coexistence curve of the phase diagram of the nuclear matter, albeit in reduced form. These points were constructed by performing the sums in Eqs. (48) and (49).

The open circles in Fig. 17 show the liquid branch, which was determined as follows. First, the vapor branch (open squares in Fig. 17) was fit to Guggenheim's universal function describing the reduced $\rho_{l,v}/\rho_c$–T/T_c coexistence curve [92],

$$\frac{\rho_{l,v}}{\rho_c} = 1 + d_1\varepsilon \pm d_\beta\varepsilon^\beta, \tag{50}$$

where ε is given by Eq. (17). The fit was performed for $0.55T_c \leqslant T \leqslant T_c$, which is roughly the range over which Guggenheim's function describes dozens of fluids (roughly from the triple point to the critical point for those fluids) [92]. The coefficients d_1 and d_β were left as fit parameters and β is a critical exponent and was taken to be [24,93]

$$\beta = \frac{\tau - 2}{\sigma} = 0.3265 \pm 0.0001. \tag{51}$$

The vapor branch is described by Eq. (50) with the minus sign and the liquid branch is described by Eq. (50) with the plus sign.

The solid curve in Fig. 17 shows the result when the open squares (vapor branch) were fit with Eq. (50), which resulted in $d_1 = 0.04315 \pm 0.00001$ and $d_\beta = 1.15714 \pm 0.00001$; the errors quoted are those resulting from the fitting procedure. These values are different from those that Guggenheim found, but that is true for other fluids as well, e.g., helium and mercury [94]. However, Eq. (50) still describes the coexistence curve of those fluids, albeit with different values for d_1 and d_β.

For all of the fluids that Guggenheim examined, the liquid branch (for the range $0.55T_c \leqslant T \leqslant T_c$) was described by Eq. (50) with the sign of d_β changed. The solid curve shown with $T/T_c > 1$ in Fig. 17 shows the result.

Dashed curves in Fig. 17 show extrapolations for $T < 0.55T_c$. The extrapolation for the vapor branch shows unphysical behavior with $\rho_v/\rho_c < 0$ for $T/T_c < 0.25$, thus some care must be taken when determining the ρ_l/ρ_c–T/T_c coexistence curve at low temperatures.

The ρ_v/ρ_c–T/T_c coexistence curve at low temperatures has already been determined from Eqs. (48) and (49). To determine the liquid branch of the coexistence curve for low temperatures we start with the the law of rectilinear diameter [92], which is

$$\frac{\rho_l + \rho_v}{2\rho_c} = 1 + d_1\varepsilon. \tag{52}$$

We extrapolated this linear function in ε from $T = 0.55T_c$ to $T = 0$. This is shown by the dashed line in Fig. 17. We then used that extrapolation and the values of ρ_v/ρ_c computed via the sums in Eqs. (48) and (49) (open squares in Fig. 17) to solve for ρ_l/ρ_c at low temperatures by "reflecting" them about the line defined by Eq. (52). Thus

$$\frac{\rho_l}{\rho_c} = 2 + 2d_1\varepsilon - \frac{\rho_v}{\rho_c}. \tag{53}$$

The results are shown by open squares in Fig. 17. The error bars on ρ_l/ρ_c are equal to the error bars on ρ_v/ρ_c.

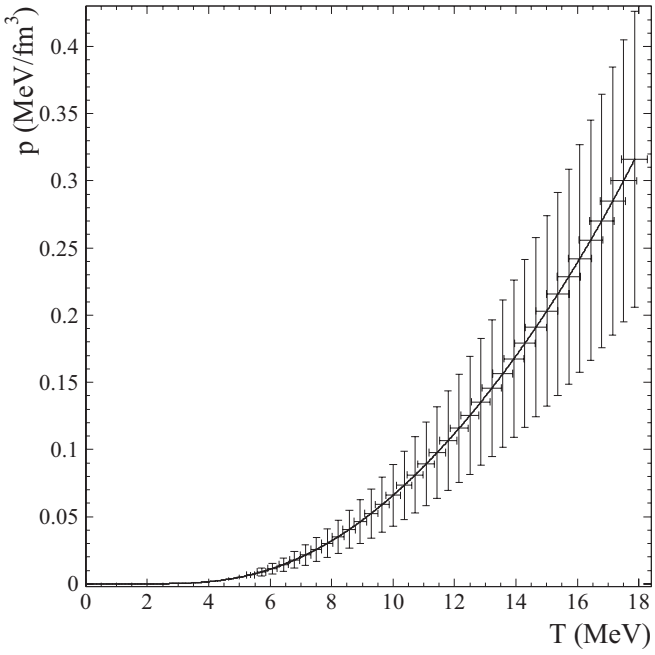

FIG. 19. Pressure-temperature coexistence curve for bulk nuclear matter. Errors are shown for selected points to give an idea of the error in the entire coexistence curve.

B. Density

To obtain a $\rho_{l,v}$-T coexistence curve in a nonreduced form (e.g., temperature in units of MeV and density in units of nucleons/fm^3) we first multiplied the temperature axis by T_c. Errors in the temperature scale are then given by

$$\delta T = \delta T_c \left(\frac{T}{T_c} \right). \tag{54}$$

To determine the density (in units of nucleons/fm)^3, we note that at $T = 0$ the density of nuclear matter should be the density observed in unexcited nuclei. Using the same value of $r_0 = 1.2181$ fm as in Eq. (22), which is within 2% of the leading order of other estimates [18], the density of nuclear matter at $T = 0$ is

$$\rho_l\,(T = 0) = \frac{3}{4\pi r_0^3} \approx 0.132 \text{ nucleons/fm}^3. \tag{55}$$

That value sets the scale on the density axis. The results are shown in Fig. 18. Different choices for the value of nuclear matter at $T = 0$ lead to different estimates of the critical density of the bulk nuclear matter.

The error bars shown in Fig. 18 are not the same as the error bars shown in Fig. 17. Simply translating the errors from Fig. 17 would give no estimate of the error of the critical density, as, by definition, there is no error associated with ρ_c/ρ_c. Therefore, we did the following: the error in a density value at a given temperature value $\rho(T)$ is

$$\delta\rho(T) = \frac{|\rho(T + \delta T) - \rho(T - \delta T)|}{2}. \tag{56}$$

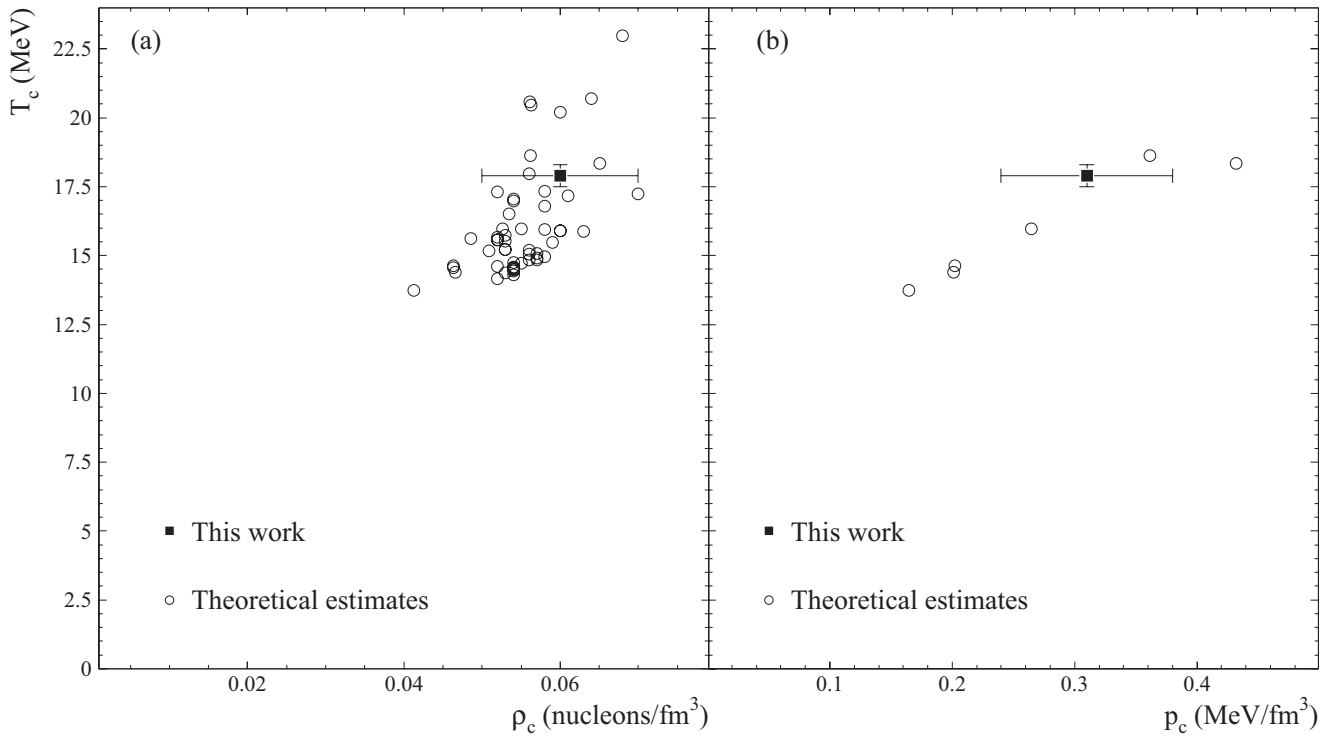

FIG. 20. Estimates for the critical point of bulk nuclear matter taken from Table III: (a) critical temperature, T_c, as a function of critical density, ρ_c; (b) critical temperature as a function of critical pressure, p_c. Open circles show the theoretical estimates listed in Table III. Filled squares show the estimates from this work.

Then we have a critical density value of $\rho_c = 0.06 \pm 0.02$ nucleons/fm^3, which agrees with some of the theoretical efforts [86–90]. There is more discussion with comparison to theory below.

Figure 18 suggests that the nuclei in the experiments analyzed in this work undergo little expansion. Table I shows that the highest excitation energy considered is $E_s^* = 4.75$ MeV/nucleon, which leads to a temperature of approximately 7.2 MeV when using Eqs. (20) and (21). This suggests that the lowest density for the nuclei considered here is approximately 96% of the density of nuclear matter at $T = 0$. This is consistent with the use of the parameters in Eq. (22) for nuclear matter at normal density and the radii used in the Coulomb interaction energy and estimates of the angular momentum.

C. Pressure

To determine the coexistence curve for pressure as a function of temperature, we again started with the reduced quantities and obtained p/p_c as a function of T/T_c by performing the sums in Eqs. (46) and (47). We then determined the value of p_c from the compressibility at the critical point, which is defined as

$$Z_c = \frac{p_c}{\rho_c T_c}. \tag{57}$$

For fluids this is a universal quantity and is $Z_c = 0.277 \pm 0.004$.

Combing Eqs. (47), (49), and (57) shows that the compressibility at the critical point is just a ratio of two Riemann ζ functions [48]:

$$Z_c = \frac{\zeta(\tau - 1)}{\zeta(\tau)} = 0.276. \tag{58}$$

However, using the error in τ [given below Eq. (26)] gives $Z_c = 0.28 \pm 0.01$. We used this value of Z_c in combination with the values of T_c and ρ_c determined above to obtain a value for the pressure at the critical point of 0.31 ± 0.07 MeV/fm^3, which agrees with some of the theoretical results [87,88]. There is more discussion of comparison with theory below. Here the error arise from the errors in T_c and ρ_c.

To obtain the pressure (in units of MeV/fm^3) we multiplied p/p_c by the value of p_c obtained above. The error in the pressure is given by

$$\delta p = \delta p_c \frac{p}{p_c}. \tag{59}$$

Figure 19 shows these results.

VI. COMPARISON WITH THEORY

There are numerous theoretical efforts that make predictions for the critical point and the liquid-vapor coexistence curve of nuclear matter [85–91]. Some, but certainly not all, of the results of these numerous theoretical efforts are compiled in Table III and shown in Fig. 20.

TABLE III. Estimates for the critical point of bulk nuclear matter in order of T_c value. The name of the model used is also given when applicable. Where no estimate was provided there is no entry in the table.

Reference model	T_c (MeV)	ρ_c (nucleons/fm^3)	p_c (MeV/fm^3)
[90] ZR1	22.98	0.068	
[90] ZR2	20.69	0.064	
[89] PRC45	20.59	0.0561	
[89] SIII	20.47	0.0563	
[90] SI	20.20	0.060	
[88] NL2	18.63	0.0562	0.3616
[88] Walecka	18.34	0.0651	0.4317
[90] SIII	17.96	0.056	
This work	17.9 ± 0.4	0.06 ± 0.01	0.31 ± 0.07
[85]	17.5 ± 1		
[90] SJ1	17.34	0.058	
[86]	17.3	0.052	
[90] SV	17.24	0.070	
[90] D250	17.16	0.061	
[90] T6	17.04	0.054	
[90] SkT4	16.98	0.054	
[90] D300	16.80	0.058	
[89] SLy230a	16.52	0.0535	
[90] ZR3	15.96	0.055	
[88] NLSH	15.96	0.0526	0.2644
[90] D1M	15.95	0.058	
[90] D1	15.90	0.060	
[91]	15.9		
[90] D1S	15.89	0.060	
[90] D1P	15.88	0.063	
[90] SkT5	15.74	0.053	
[90] SkP	15.67	0.052	
[89] TM1	15.62	0.0486	
[90] SkO	15.57	0.052	
[90] SkOp	15.56	0.052	
[90] BSk17	15.53	0.053	
[90] D260	15.48	0.059	
[90] Gs	15.21	0.053	
[90] Rs	15.21	0.053	
[90] SkI1	15.20	0.056	
[89] TW	15.18	0.0509	
[90] SkI4	15.08	0.057	
[90] SGI	15.05	0.056	
[90] SkI3	14.97	0.058	
[90] LNS	14.92	0.057	
[90] SkI6	14.85	0.056	
[90] SkI5	14.83	0.057	
[90] SkI2	14.74	0.054	
[90] RATP	14.72	0.055	
[88] NL3	14.64	0.0463	0.2020
[90] SkM?	14.61	0.052	
[90] SLy0	14.58	0.054	
[90] SLy1	14.55	0.054	
[90] SLy3	14.55	0.054	
[90] SLy5	14.55	0.054	
[89] NL3	14.55	0.0463	
[90] SLy230a	14.54	0.054	

TABLE III. (*Continued*).

Reference model	T_c (MeV)	ρ_c (nucleons/fm^3)	p_c (MeV/fm^3)
[90] SLy8	14.54	0.054	
[90] SLy4	14.52	0.054	
[90] SLy6	14.48	0.054	
[90] SLy7	14.44	0.054	
[87]	14.4	0.04661	0.2010
[90] SLy2	14.37	0.053	
[90] SkMP	14.29	0.054	
[90] SLy9	14.16	0.052	
[88] NL1	13.74	0.0413	0.1644

There are two theoretical estimates of T_c that agree with our estimate to within error bars: the SIII model in Refs. [85] and [90]. There are 13 other theoretical estimates within 10% of our measurement. All but five theoretical estimates of ρ_c agree to within error bars with our estimate. There are two theoretical estimates of p_c that agree with our estimate: the NL2 model [88] and the NLSH model [88].

Figure 2 in Ref. [88] and Fig. 8 in Ref. [90] show reduced density-reduced temperature coexistence curves such as the one shown in Fig. 17 here. A visual inspection of the figures in those references shows that only the curves from the Walecka model [88] and the ZR1 and SV models [90] have the symmetry observed in the reduced density-reduced temperature coexistence curve shown in Fig. 17.

Based on the above-mentioned agreement of the values of the critical point and the shape of the reduced density-reduced temperature coexistence curve, it is clear that the results presented in this work agree best with the results of the SV model [90], though many other models and theories do well.

VII. SUMMARY

The aim of this paper was to extract that liquid-vapor phase diagram of infinite, uncharged, symmetric nuclear matter from the data measured in various nuclear reaction experiments using finite, charged, asymmetric nuclear matter, i.e., atomic nuclei. Because the usual thermodynamical methods are obviously not accessible in this case, we concentrated on the fragment charge distributions at various excitation energies and analyzed them according to Fisher's droplet model modified to account for the finite size of the system and the nuclear nature of the fluid (e.g., isospin and Coulomb effects).

By fitting the charge yields observed in six different reactions studied in three experiments, the critical point was found to be $T_c = 17.9 \pm 0.4$ MeV, $\rho_c = 0.06 \pm 0.02$ nucleons/fm^3, and $p_c = 0.31 \pm 0.07$ MeV/fm^3. Using the critical temperature and assuming that the formation of fragments exhausts all nonidealities, the entire coexistence curve of bulk nuclear matter was determined from $T = 0$ to the critical point. This represents the first experimental measure of the phase diagram of bulk nuclear matter. It is likely that the ideas and techniques outlined in this work would be useful in mapping other areas of the phase diagram of nuclear matter such as the phase transition between hadronic matter and the quark gluon plasma.

ACKNOWLEDGMENTS

This work was performed by Lawrence Berkeley National Laboratory and was supported by the Director, Office of Energy Research, Office of High Energy and Nuclear Physics, Division of Nuclear Physics, of the U.S. Department of Energy under Contract No. DE-AC02-05CH11231. LLNL-JRNL-539511. This work was also performed under the auspices of the U.S. Department of Energy by Lawrence Livermore National Laboratory under Contract DE-AC52-07NA27344. The authors would like to thank the members of the EOS and ISiS Collaborations for access to their excellent experimental data sets.

[1] J. E. Finn *et al.*, Phys. Rev. Lett. **49**, 1321 (1982).
[2] P. J. Siemens, Nature **305**, 410 (1983).
[3] A. S. Hirsch *et al.*, Phys. Rev. C **29**, 508 (1984).
[4] M. L. Gilkes *et al.*, Phys. Rev. Lett. **73**, 1590 (1994).
[5] J. Pochodzalla *et al.*, Phys. Rev. Lett. **75**, 1040 (1995).
[6] X. Campi and H. Krivine, Nucl. Phys. A **620**, 46 (1997).
[7] L. G. Moretto *et al.*, Phys. Rep. **287**, 249 (1997).
[8] A. Bonasera *et al.*, Riv. Nuovo Cimento **23**, 1 (2000).
[9] M. DAgostino *et al.*, Phys. Lett. B **473**, 219 (2000).
[10] J. B. Elliott *et al.*, Phys. Rev. C **62**, 064603 (2000).
[11] J. B. Elliott *et al.*, Phys. Rev. Lett. **88**, 042701 (2002).
[12] M. Kleine Berkenbusch *et al.*, Phys. Rev. Lett. **88**, 022701 (2001)
[13] B. K. Srivastava *et al.*, Phys. Rev. C **65**, 054617 (2002).
[14] M. DAgostino *et al.*, Nucl. Phys. A **650**, 328 (1999).
[15] L. G. Moretto, R. Ghetti, L. Phair, K. Tso, and G. J. Wozniak, Phys. Rev. Lett. **76**, 2822 (1996).
[16] J. B. Elliott and A. S. Hirsch, Phys. Rev. C **61**, 054605 (2000).
[17] C. F. v. Weizsäcker, Z. Phys. A **96**, 431 (1935).
[18] W. D. Myers and W. J. Świątecki, Phys. Rev. C **62**, 044610 (2000).
[19] G. Royer and C. Gautier, Phys. Rev. C **73**, 067302 (2006).
[20] V. Weisskopf, Phys. Rev. **52**, 295 (1937).
[21] L. G. Moretto, J. B. Elliott, and L. Phair, Phys. Rev. C **72**, 064605 (2005).
[22] L. G. Moretto, K. A. Bugaev, J. B. Elliott, R. Ghetti, J. Helgesson, and L. Phair, Phys. Rev. Lett. **94**, 202701 (2005).
[23] L. G. Moretto, J. B. Elliott, and L. Phair, Phys. Rev. C **68**, 061602(R) (2003).
[24] M. E. Fisher, Physics (N.Y.) **3**, 255 (1967).
[25] M. E. Fisher, Rep. Prog. Phys. **30**, 615 (1967).
[26] Y. G. Ma *et al.*, Phys. Rev. C **71**, 054606 (2005).
[27] T. S. Fan *et al.*, Nucl. Phys. A **679**, 121 (2000).
[28] Z. Q. Xie *et al.*, Rev. Sci. Instrum. **62**, 775 (1991).
[29] M. A. McMahan *et al.*, Nucl. Instrum. Methods A **253**, 1 (1986).

[30] K. X. Jing *et al.*, Nucl. Phys. A **645**, 203 (1999).
[31] J. Aichlen, Phys. Rep. **202**, 233 (1991).
[32] J. B. Bondorf *et al.*, Phys. Rep. **257**, 133 (1995).
[33] D. H. E. Gross, Phys. Rep. **279**, 119 (1997).
[34] J. Richert and P. Wagner, Phys. Rep. **350**, 1 (2001).
[35] P. Chomaz, M. Colonna, and J. Randrup, Phys. Rep. **389**, 263 (2004).
[36] C. B. Das *et al.*, Phys. Rep. **406**, 1 (2005).
[37] V. E. Viola *et al.*, Phys. Rep. **434**, 1 (2006).
[38] J. A. Hauger *et al.*, Phys. Rev. Lett. **77**, 235 (1996).
[39] J. A. Hauger *et al.*, Phys. Rev. C **62**, 024616 (2000).
[40] J. B. Elliott *et al.*, Phys. Rev. C **67**, 024609 (2003).
[41] G. Rai *et al.*, IEEE Trans. Nucl. Sci. **37**, 56 (1990).
[42] W. Christie *et al.*, Nucl. Instrum. Methods Phys. Res. Sec. A **255**, 46 (1987).
[43] K. Kwiatkowski, Nucl. Instrum. Methods Phys. Res. Sec. A **360**, 571 (1995).
[44] T. Lefort *et al.*, Phys. Rev. Lett. **83**, 4033 (1999).
[45] L. Beaulieu *et al.*, Phys. Rev. Lett. **84**, 5971 (2000).
[46] L. Beaulieu *et al.*, Phys. Rev. C **63**, 031302 (2001).
[47] C. M. Mader, A. Chappars, J. B. Elliott, L. G. Moretto, L. Phair, and G. J. Wozniak, Phys. Rev. C **68**, 064601 (2003).
[48] C. S. Kiang, Phys. Rev. Lett. **24**, 47 (1970).
[49] W. Rathjen *et al.*, Phys. Lett. A **40**, 345 (1972).
[50] D. Saltz, J. Chem. Phys. **101**, 6038 (1994).
[51] D. Stauffer *et al.*, Phys. Rev. B **6**, 2780 (1972).
[52] A. Dillmann and G. E. A. Meier, J. Chem. Phys. **94**, 3872 (1991).
[53] J. E. Mayer and M. G. Mayer, *Statistical Mechanics* (John Wiley, New York, 1940).
[54] J. Frenkel, *Kinetic Theory of Liquids* (Oxford University Press, New York, 1946).
[55] D. Stauffer and C. S. Kiang, Adv. Colloid Interface Sci. **7**, 1031977).
[56] M. E. Fisher and M. F. Sykes, Phys. Rev. **114**, 45 (1959).
[57] E. Stoll *et al.*, Phys. Rev. B **6**, 2777 (1972).
[58] D. Stauffer, Phys. Rep. **54**, 1 (1979).
[59] J. L. Cambier and M. Nauenberg, Phys. Rev. B **34**, 8071 (1986).
[60] W. Bauer, Phys. Rev. C **38**, 1297 (1988).
[61] J. Kertész, Physica A **161**, 58 (1989).
[62] J. S. Wang, Physica A **161**, 249 (1989).
[63] J. S. Wang and R. H. Swendsen, Physica A **167**, 565 (1990).
[64] J. B. Elliott *et al.*, Phys. Rev. C **49**, 3185 (1994).
[65] V. Latora *et al.*, Nucl. Phys. A **572**, 477 (1994).
[66] V. Latora, M. Belkacem, and A. Bonasera, Phys. Rev. Lett. **73**, 1765 (1994).
[67] S. Pratt, Phys. Lett. B **349**, 261 (1995).
[68] M. Belkacem, V. Latora, and A. Bonasera, Phys. Rev. C **52**, 271 (1995).
[69] P. Finocchiaro *et al.*, Nucl. Phys. A **600**, 236 (1996).
[70] S. Das Gupta, J. Pan, and M. B. Tsang, Phys. Rev. C **54**, R2820 (1996).
[71] A. Strachan and C. O. Dorso, Phys. Rev. C **55**, 775 (1997).
[72] J. B. Elliott *et al.*, Phys. Rev. C **55**, 1319 (1997).
[73] V. N. Kondratyev *et al.*, J. Chem. Phys. **106**, 7766 (1997).
[74] J. M. Carmona *et al.*, Nucl. Phys. A **643**, 115 (1998).
[75] A. Strachan and C. O. Dorso, Phys. Rev. C **59**, 285 (1999).
[76] F. Gulminelli and Ph. Chomaz, Phys. Rev. Lett. **82**, 1402 (1999).
[77] C. O. Dorso, V. C. Latora, and A. Bonasera, Phys. Rev. C **60**, 034606 (1999).
[78] J. B. Elliott *et al.*, Phys. Rev. Lett. **85**, 1194 (2000).
[79] J. B. Elliott, L. G. Moretto, and L. Phair, Phys. Rev. C **71**, 024607 (2005).
[80] K. Hagel *et al.*, Nucl. Phys. A **486**, 429 (1988).
[81] A. H. Raduta and A. R. Raduta, Phys. Rev. C **55**, 1344 (1997).
[82] K. Summerer, W. Bruchle, D. J. Morrissey, M. Schadel, B. Szweryn, and W. Yang, Phys. Rev. C **42**, 2546 (1990).
[83] S. K. Blau and L. G. Moretto, Nucl. Phys. A **359**, 477 (1981).
[84] J. B. Natowitz *et al.*, Int. J. Mod. Phys. E **13**, 269 (2004).
[85] B. Friedman and V. R. Pandharipande, Nucl. Phys. A **361**, 502 (1981).
[86] N. K. Glendenning, L. P. Csernai, and J. I. Kapusta, Phys. Rev. C **33**, 1299 (1986).
[87] H. Müller and B. D. Serot, Phys. Rev. C **52**, 2072 (1995).
[88] J. B. Silva *et al.*, Phys. Lett. B **664**, 246 (2008).
[89] M. Dutra, O. Lourenco, A. Delfino, J. S. Sá Martins, C. Providencia, S. S. Avancini, and D. P. Menezes, Phys. Rev. C **77**, 035201 (2008).
[90] A. Rios, Nucl. Phys. A **845**, 58 (2010).
[91] M. Jin, M. Urban, and P. Schuck, Phys. Rev. C **82**, 024911 (2010).
[92] E. A. Guggenheim, J. Chem. Phys. **13**, 253 (1945).
[93] M. Campostrini, A. Pelissetto, P. Rossi, and E. Vicari, Phys. Rev. E **65**, 066127 (2002).
[94] M. Ross and F. Hensel, J. Phys.: Condens. Matter **8**, 1909 (1996).